JGR Oceans

RESEARCH ARTICLE
10.1029/2021JC017363

Hydrate Formation on Marine Seep Bubbles and the Implications for Water Column Methane Dissolution

X. Fu[1], W. F. Waite[2], and C. D. Ruppel[2]

[1]Department of Mechanical and Civil Engineering, California Institute of Technology, Pasadena, CA, USA, [2]U. S. Geological Survey, Woods Hole, MA, USA

Key Points:

- In deepwater marine environments, some methane bubbles emerging from the seafloor acquire gas hydrate shells before they release
- Gas hydrate shells form when bubble release rates from seeps within the hydrate stability zone are slower than ~10 s per bubble
- Within 1.5 m of rise, most bubbles grow shells, with initially shelled bubbles having ~5% more gas than initially clean bubbles

Supporting Information:

Supporting Information may be found in the online version of this article.

Correspondence to:

X. Fu,
rubyfu@caltech.edu

Citation:

Fu, X., Waite, W. F., & Ruppel, C. D. (2021). Hydrate formation on marine seep bubbles and the implications for water column methane dissolution. *Journal of Geophysical Research: Oceans*, *126*, e2021JC017363. https://doi.org/10.1029/2021JC017363

Received 15 MAR 2021
Accepted 11 AUG 2021

Abstract Methane released from seafloor seeps contributes to a number of benthic, water column, and atmospheric processes. At seafloor seeps within the methane hydrate stability zone, crystalline gas hydrate shells can form on methane bubbles while the bubbles are still in contact with the seafloor or as the bubbles begin ascending through the water column. These shells reduce methane dissolution rates, allowing hydrate-coated bubbles to deliver methane to shallower depths in the water column than hydrate-free bubbles. Here, we analyze seafloor videos from six deepwater seep sites associated with a diverse range of bubble-release processes involving hydrate formation. Bubbles that grow rapidly are often hydrate-free when released from the seafloor. As bubble growth slows and seafloor residence time increases, a hydrate coating can form on the bubble's gas-water interface, fully coating most bubbles within ~10 s of the onset of hydrate formation at the seafloor. This finding agrees with water-column observations that most bubbles become hydrate-coated after their initial ~150 cm of rise, which takes about 10 s. Whether a bubble is coated or not at the seafloor affects how much methane a bubble contains and how quickly that methane dissolves during the bubble's rise through the water column. A simplified model shows that, after rising 150 cm above the seafloor, a bubble that grew a hydrate shell before releasing from the seafloor will have ~5% more methane than a bubble of initial equal volume that did not grow a hydrate shell after it traveled to the same height.

Plain Language Summary Methane is the primary component of natural gas. Processes that affect the formation, consumption, and redistribution of methane in natural settings have significant environmental consequences, such as ocean acidification and greenhouse warming. In water deeper than 500–600 m, methane bubbles can acquire shells of gas hydrate, a crystalline solid made of methane and water molecules. Here, we study how the process of hydrate shell formation alters the fate of methane that naturally bubbles up from the seafloor. We find that bubbles taking longer than ~10 s to release at seafloor that is within the local methane hydrate stability often grow hydrate shells before rising into the water column. As bubbles ascend through the water column, the hydrate shells slow down bubble dissolution and gas exchange, allowing more methane to be delivered to shallower water depths.

1. Introduction

Methane is an environment-altering molecule, function as a fuel for human activities, a carbon source for benthic, water-column, and wetland ecosystems (Levin, 2005; Valentine et al., 2001), and a greenhouse gas in the atmosphere (Sundquist & Visser, 2003). Assessing methane's impact on contemporary and future climate, ecosystems, and ocean chemistry requires tracking and quantifying methane migration through the natural environment.

In marine systems, methane has a complex role and history. Below the seafloor, methane is primarily produced either by microbes that consume buried organic matter in shallow sediments or by thermal breakdown of organic carbon at greater depths (Reeburgh, 2007; Whiticar, 1999). Once produced, methane may be dissolved in sediment pore waters, exist in the vapor phase between sediment grains or in fractures, or combine with water to form solid gas hydrate under certain pressure and temperature conditions (e.g., Ruppel & Waite, 2020). Methane that finds a pathway for upward migration through the sedimentary section is mostly consumed by anaerobic oxidation of methane (AOM) before reaching the seafloor (Reeburgh, 1976). However, rapid advection of methane through sediments can effectively overwhelm the AOM sink (Joye et al., 2004; Orcutt et al., 2005), allowing methane to be emitted from seafloor seeps as bubbles.

To maintain its pressure equilibrium with the surrounding water, a gas bubble will expand as it rises, depressurizing as the surrounding water pressure decreases with decreasing depth. Leifer and Patro (2002) note, however, that bubbles also seek to equilibrate chemically with the surrounding waters, and that a rapid net diffusion of gas out of the bubble can cause the bubble to shrink rather than expand as it rises. Because oceanic dissolved methane concentrations are typically low relative to their solubility or equilibrium concentrations (Ruppel & Kessler, 2017), methane diffuses out of bubbles so rapidly that methane bubbles are observed to shrink as they rise (Rehder et al., 2002, 2009). The diffusive loss of methane from bubbles is rapid enough that, once released at the seafloor, typical bubbles are completely stripped of their methane during the first ~100 m of the bubble's ascent (McGinnis et al., 2006). The dissolved, bubble-derived methane is consumed in the deep ocean (Leonte et al., 2018) during microbially mediated aerobic oxidation (Valentine et al., 2001) that leaves a byproduct of carbon dioxide, which in turn may contribute to ocean acidification (Garcia-Tigreros et al., 2021; Garcia-Tigreros & Kessler, 2018; Reeburgh, 2007). Analysis of dissolved methane in the near-surface ocean in deepwater areas confirms that very little can be traced to seafloor emissions (Leonte et al., 2020; Sparrow et al., 2018). Instead, most methane in the near-surface ocean proximal to seafloor seeps appears to be produced *in situ* by plankton (Leonte et al., 2020; Pohlman et al., 2017), and enhanced sea-air methane flux traceable to seafloor methane emissions has not been found in deepwater seep provinces surveyed to date (e.g., Myhre et al., 2016).

This article focuses on the fate of methane bubbles emitted from the seafloor at locations where the local pressure and temperature conditions are within the hydrate stability zone. It has long been postulated that such bubbles may form enclosing shells of gas hydrate that could reduce the diffusion of methane into the surrounding water during the bubble's ascent, thereby allowing the methane to reach shallower depths in the water column before dissolution occurs. This hypothesis was further supported by field experiments (Rehder et al., 2002) and later theorized into models (McGinnis et al., 2006), which suggest that a hydrate shell can slow the rate of transport of methane out of a bubble by 80%. Thus, establishing how and when a bubble might grow a hydrate shell has significant implications for methane transport through the water column. With the increasing number of remotely operated vehicle (ROV) explorations of seafloor methane seeps, substantial direct observational data have accumulated to document the rate and pattern of hydrate formation around methane bubbles at and near the seafloor. Here, we combine theoretical constraints with the quantitative analyses of seafloor videos collected at deepwater seeps on North American continental margins to determine the characteristics of bubbles that are most likely to acquire hydrate coatings and to assess the impact of hydrate shells on the preservation of methane within bubbles.

2. Background

The amount of methane emitted from the seafloor into the overlying ocean is estimated to lie in the broad range of 16–3,200 Tg yr^{-1} based on mass balance considerations that take into account the contemporary concentration of methane in the oceans and aerobic methane oxidation in the water column (Ruppel & Kessler, 2017). There are few reliable bottom-up estimates for global methane emissions into the ocean, mostly because the number and distribution of deepwater methane seeps and their flux are so poorly constrained (Phrampus et al., 2020; Skarke et al., 2014). Hovland et al. (1993) estimate 8–65 Tg methane (CH_4) per year emitted from seeps on global continental shelves. That study, however, focused on a setting where water depths are too shallow and water temperatures too high for gas bubbles to acquire the hydrate shells that are the focus of this article. Kvenvolden et al. (2001) gave an estimate of 20 Tg CH_4 yr^{-1} emissions into the water column from seafloor seeps at a time when widespread seafloor seepage had been described mostly in petroleum basins (Bernard et al., 1976; Cranston et al., 1994). Recent discoveries made using modern acoustic and mapping techniques suggest that seafloor methane seeps are a common occurrence along deepwater global continental margins (Boetius & Wenzhöfer, 2013; Johnson et al., 2015; Riedel et al., 2018; Ruppel & Kessler, 2017; Skarke et al., 2014; Westbrook et al., 2009) and are likely to number in the tens of thousands worldwide (Boetius & Wenzhöfer, 2013; Phrampus et al., 2020).

As noted above, most vapor phase methane released from the seafloor as bubbles at water depths exceeding ~100 m (McGinnis et al., 2006) diffuses into the water column and is consumed by microbial aerobic oxidizers, a process that depletes both the dissolved methane and the water column's oxygen and leaves behind carbon dioxide (Heintz et al., 2012; Valentine et al., 2001). Microbial communities respond rapidly

to changes in dissolved methane concentrations (Redmond & Valentine, 2012), even consuming nearly all of the methane released during the Deepwater Horizon incident (Kessler et al., 2011).

The water depth at which microbial oxidation is most active strongly depends on the availability of dissolved methane, which is controlled by three parameters: (a) the mass transfer rate across the surface of ascending methane bubbles, which describes how rapidly methane dissolves into the water; (b) the rise velocity of the bubble, which influences the vertical scale of methane dissolution into the water column and potentially the atmosphere; and (c) the methane mass fraction (or partial pressure) in a bubble, which controls how much methane is available at the bubble's surface for dissolution (e.g., Leifer & Patro, 2002; Li & Huang, 2016; McGinnis et al., 2006; Topham, 1984a; Wang et al., 2020; Yapa et al., 2010). All three parameters change when a gas hydrate shell grows around the methane bubble (see Sections 5.1 and 5.2). Where seafloor pressure-temperature conditions are within the hydrate stability zone, hydrate shells may grow around emitted bubbles either while the bubbles are still attached to the seafloor or soon after they are released from the seafloor. Understanding the processes related to bubble release at seafloor seeps, the growth of hydrate shells, and the evolution of bubbles in the water column is essential for quantifying how methane released from the seafloor becomes distributed throughout the water column.

In the deep ocean, gas hydrate formation is often limited by methane availability, even when the *P-T* conditions are well within the gas hydrate stability field (Ruppel & Waite, 2020). As reviewed by Ruppel and Kessler (2017), the ocean as a whole is greatly undersaturated in methane, and a bubble exposed to water depleted in methane begins dissolving via methane diffusion across the bubble-water interface even under favorable hydrate-forming conditions (Chen et al., 2014; Maini & Bishnoi, 1981; Rehder et al., 2002, 2009; Warzinski et al., 2014). With time, however, methane dissolution from the bubble increases the dissolved methane content in a thin boundary layer of water around the gas-water interface and can promote hydrate formation (Boewer et al., 2012) on the bubble's surface. At the gas-water interface, localized competition between the rates of methane diffusion and hydrate nucleation determines whether a hydrate layer can eventually form. When the driving force for hydrate nucleation increases, such as in deeper and colder waters that are far within the hydrate stability field, hydrate nucleation rates can outpace the rate of methane diffusion, and macroscopic hydrate formation can occur even in methane-poor environments (Chen et al., 2014; Maini & Bishnoi, 1981).

The formation of gas hydrate on emitted gas bubbles is favored where ocean waters have higher concentrations of methane, even if the concentrations are still significantly below methane saturation. Elevated dissolved methane concentrations have been measured near the seafloor above continental slope methane seeps in many settings, including the United States Atlantic, Cascadia, Gulf of Mexico (GOM), and Svalbard margins (Garcia-Tigreros et al., 2021; Graves et al., 2015; Lapham et al., 2013; Thomsen et al., 2012). Close to seafloor seeps, dissolved methane concentrations can be two to seven orders of magnitude (Lapham et al., 2013; Thomsen et al., 2012) larger than the background value for deep ocean waters (~2.5–3.5 nM; Rehder et al., 1999).

Water column observations and laboratory measurements (Maini & Bishnoi, 1981; Wang et al., 2016; Warzinski et al., 2014) have described the rapid formation of hydrate shells on rising bubbles, but less is known about when and how such coatings initiate and grow on bubbles emitted from natural seeps. Existing bubble rise models (Topham, 1984b) and the family of models (Li & Huang, 2016; McGinnis et al., 2006; Wang et al., 2020; Yapa et al., 2010) based on the experimental results of Rehder et al. (2002, 2009), assume that bubbles released at the seafloor are initially hydrate-free and grow hydrate shells after some elapsed time. McGinnis et al. (2006) parameterize this transition by assuming the hydrate shell only forms once the bubble diameter shrinks to 3.5 mm during the bubble's ascent. With this assumption, McGinnis et al. (2006) conclude that a Black Sea bubble plume (flare) detectable at 1,300 m above the seafloor would require bubbles to be 20 mm in diameter when emitted. Not only do bubbles of this size tend to break into smaller bubbles (McGinnis et al., 2006), but Black Sea bubble sizes are mostly in the range of 1.4–18.2 mm diameter (Egorov et al., 2003), with an average emission diameter of 6 mm (McGinnis et al., 2006). If the bubbles are instead initially assumed to be hydrate-coated when released from the seafloor, the bubble diameters only need to average 9 mm to create the 1,300 m-tall Black Sea flare (McGinnis et al., 2006).

In this study, we analyze seafloor videos from six natural deepwater seep sites on North American marine margins to assess the impact of hydrate shell formation on bubble release characteristics. From these videos, we classify bubbles into two general categories: (a) hydrate-free, or "clean" bubbles with fully mobile surfaces that tend to be shiny and clear; (b) hydrate-coated bubbles, for which the hydrate coating is characterized by gray or silvery, semi-rigid, or rigid surfaces. These distinctions are not always obvious, and dedicated bubble-seep research endeavors would improve on the observations made here by utilizing dual high-speed cameras (Wang & Socolofsky, 2015; Wang et al., 2016), and reference grids for size analysis (Padilla & Weber, 2021; Rehder et al., 2002).

We examine the role of local lithology, bubble release rates, and extant gas hydrate in controlling the size, shape, and nature of the hydrate coating for bubbles emitted at the seafloor. We apply a simplified model to determine the relationship between the methane content of a bubble and the fraction of the bubble that is hydrate-coated after 150 cm of rise in the water column. In the absence of any site-specific gas or water chemistry information, our simplified model assumes all bubbles are oil-free and formed purely from methane, though we do indicate how model results would vary in the presence of oil or a mixed gas with higher hydrocarbons. Our objective in this study is to couple visual observations with modeling results to show how a range of observed initial bubble conditions and methane emission processes contribute to methane dissolution in the water column over deepwater methane seeps emitting bubbles within the gas hydrate stability zone.

3. Geologic Setting

We use videos recorded during ROV dives at six actively bubbling seafloor methane seeps (Figure 1a; Table 1) to constrain seep lithology, the characteristics of bubble emissions (e.g., rate and bubble size), and the extent of hydrate coating on bubbles before they are released from the seafloor and, when possible, ~150 cm into their water column ascent. All of the seeps are located at water depths and associated with bottom water temperatures that place them within the methane hydrate stability field (Figure 1b; Table 2). The six seep sites are located on North American marine margins, including the active margin offshore Vancouver Island and on passive margins south of New England and in the salt tectonic province of the northern GOM petroleum basin. Despite the range of tectonic settings, probable gas sources, and seafloor conditions represented by these seeps, the observed bubble emission and hydrate formation processes reveal fundamental physical and chemical insights that apply regardless of seep setting. Here, we review the key characteristics and video-based observations about the six sites.

3.1. Cascadia Margin

The Barkley Canyon seep (Figure 1a, panel 1) lies on the northern part of the Cascadia active margin in the Northeast Pacific Ocean. Since 2015, over a thousand previously unknown bubble plumes have been discovered along this margin from offshore Vancouver Island to northern California at water depths of tens of meters to more than 2,500 mbsl (e.g., Embley et al., 2016; Johnson et al., 2015; Merle & Embley, 2016; Merle et al., 2021; Riedel et al., 2018). The seep we focus on here is at the NEPTUNE cabled observatory node referred to as "Barkley Canyon Axis" near the "Barkley Canyon Hydrates" node that is frequently monitored by ROVs (e.g., Juniper et al., 2013) and a remotely operated deep-sea crawler (Chatzievangelou et al., 2020; Doya et al., 2017; Purser et al., 2013). For this study, we use a 2012 ROV Ropos video described by Seabrook et al. (2019) that captures active methane seepage at 985 mbsl (Table 1), which is well within the stability field for methane hydrate (Table 2). Seep emission dynamics at this location have previously been described by Thomsen et al. (2012). In the Ropos video from Seabrook et al. (2019), the seep is producing mostly hydrate-free, clear-surfaced, "clean" gas bubbles that rapidly release from small orifices (also referred to as "emitters") in sediment that appears relatively uniform and fine-grained in the video (Text S1c). Though the video does not contain images of hydrate outcrops or bacterial mats, two slightly gray, hydrate-coated bubbles that do not release from the seafloor are visible. Additionally, gas bubbles collect under the crab on the right side of Figure 2a and begin forming hydrate. Enough gas eventually accumulates to overcome the crab's mass, lifting and flipping the crab over (Figure 2b). The hydrate detaches and begins ascending through the water column as the crab somersaults to the seafloor (Figure 2c).

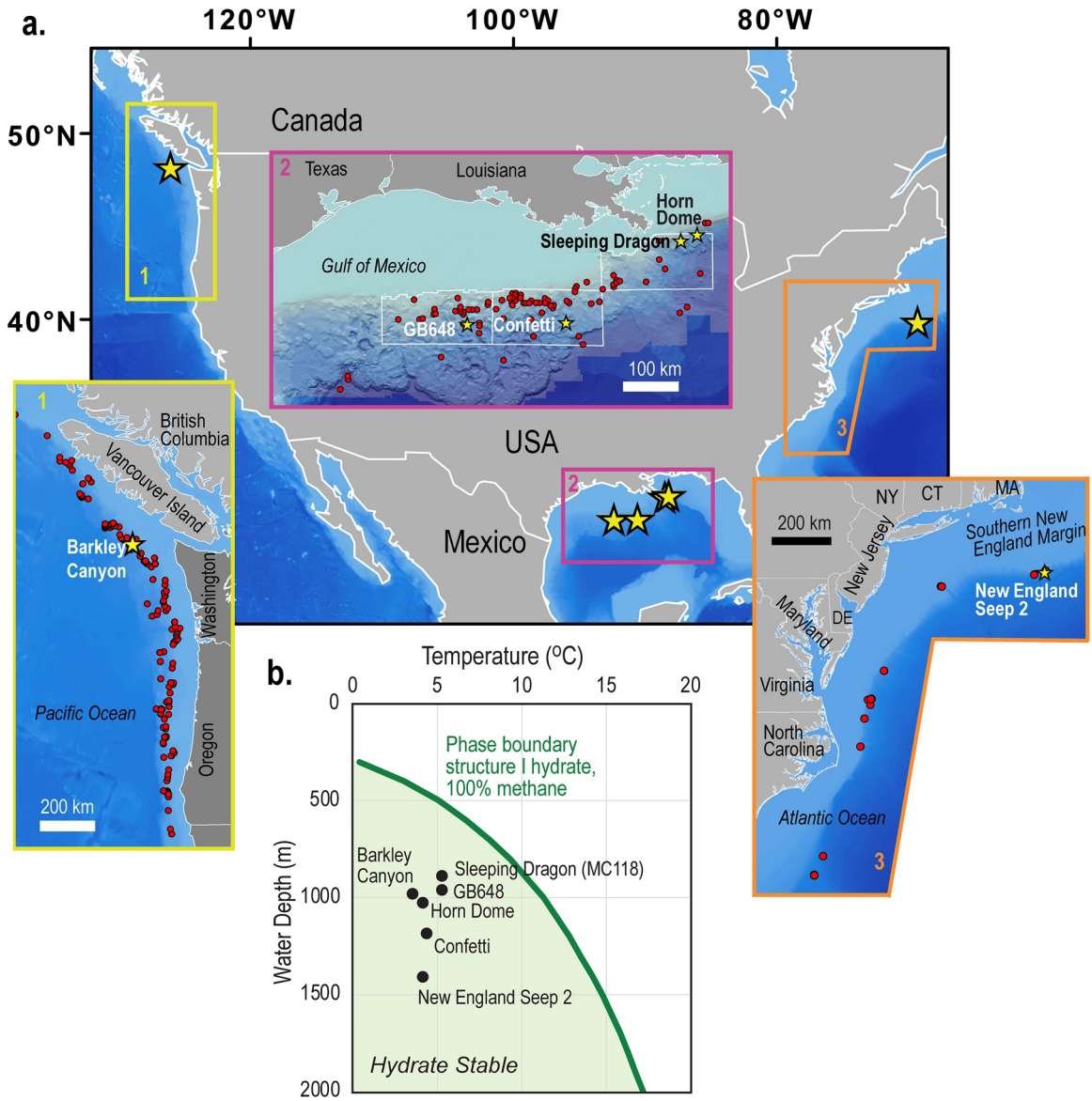

Figure 1. (a) Large map shows stars at the locations of North American margin seeps highlighted in this article. Inset 1: Cascadia margin with the location of the Barkley Canyon site and seeps (red) that have been mapped at greater than 500 mbsl (nominal top of gas hydrate stability; Ruppel & Waite, 2020) by Riedel et al. (2018), Embley et al. (2016), Merle and Embley (2016), and Merle et al. (2021). Inset 2: Northern Gulf of Mexico showing the location of GB648, Confetti, Sleeping Dragon, and Horn Dome. Seeps indicated in red are georeferenced from those shown for the continental slope from Fisher et al. (2015). From west to east, the white outlines indicate the Garden Banks, Green Canyon, and Mississippi Canyon protraction areas. Bathymetry from Kramer and Shedd (2017). Inset 3: United States Atlantic margin showing the location of New England Seep 2 and seeps (red) deeper than 550 mbsl (nominal top of gas hydrate stability) from Skarke et al. (2014). (b) Gas hydrate stability curve is shown in green for Structure I methane-only hydrate calculated for 3.5% weight percent NaCl in water using the fit to the Sloan and Koh (2007) equation as given in Table 1 of Ruppel and Waite (2020). The corresponding water depth and bottom water temperatures at each of the seep sites discussed here are indicated by the black dots. The degree of supercooling given in Table 2 is the difference between observed temperatures and the corresponding phase boundary temperature at that depth.

3.2. Northern Gulf of Mexico

Four of the seafloor seeps that we analyze are located in the northern GOM salt tectonics province (Figure 1a, panel 2), a passive margin setting that hosts one of the world's most productive marine petroleum basins. Seafloor morphology of this area is controlled by salt diapirism and faulting, with salt withdrawal basins developing between the buried salt bodies (Worrall & Snelson, 1989). Especially at basin boundaries, faults form to accommodate salt ascent through the sediment and serve as the loci for seafloor leakage of fluids (gas, petroleum, and brines). Gas hydrate systems have been recognized in the northern GOM from

Table 1
Study Site Locations and References for the Original Seafloor Videos

Site name	Latitude	Longitude	Reference
Sleeping Dragon (MC118)	28°51.1421′N	88°29.5109′W	Wang and Socolofsky (2015) Wang et al. (2016)
Garden Banks 648 (GB648)	27°20.3465′N	92°21.6182′W	Lobecker et al. (2019)
Barkley Canyon	48°19.0057′N	126°3.0098′W	Seabrook et al. (2019)
Horn Dome (MC36)	28°57.9380′N	88°11.6970′W	Kennedy et al. (2019)
Confetti (GC600)	27°22.1954′N	90°34.2624′W	Wang et al. (2016)
New England Seep 2	39°52.2625′N	69°17.1560′W	Shank et al. (2014)

Note. Lease block designations are given in parentheses for the four sites in the Gulf of Mexico. Barkley Canyon is located offshore Vancouver Island and New England Seep two is offshore Massachusetts (Figure 1). Links to site and video information are provided in Text S1–S6.

the seafloor to great depths within the sediments and at locations ranging from cold seeps to mud volcanoes to conformably deposited sediments and associated fractures in the salt withdrawal basins (Boswell et al., 2012; Brooks et al., 1984; Cook et al., 2008; Daigle et al., 2018; Hutchinson et al., 2011; Roberts, 2001). Gas mixtures emitted at northern GOM seeps may contain hydrocarbons other than methane (e.g., Brooks et al., 1984), but we analyze the bubble dynamics assuming pure methane, which is the dominant gas at some seeps (Sassen et al., 2003) and which simplifies the analyses and comparisons undertaken here. Northern GOM sites are identified by their protraction area and lease block designator.

The seep at Garden Banks 648 (GB648) was explored by *ROV Deep Discoverer* in 2014 (Lobecker et al., 2019). The site is characterized by active bubble emissions set in an area with authigenic carbonate outcrops and bare seafloor sediment. Hydrate has accumulated beneath a carbonate ledge ~10 m away from the area shown in Figure 3 (see, e.g., Figure 2; Text S2a and also Ruppel & Kessler, 2017). We consider a seafloor seep site that is covered in bacterial mats and fine-grained sediment adjacent to snails and a carbonate outcrop (Figure 3a). Bacterial mats are interpreted as being associated with higher seafloor methane fluxes (Levin, 2005; Lloyd et al., 2010), and the bubbles (Figure 3b) originate from small orifices within the bacterial mats and surrounding fine-grained sediment. Even within the small area studied here (Figure 3b), bubbles show diversity in size, shape and fractional hydrate coverage.

Horn Dome (HD) (Figures 1 and 4, inset), located in Mississippi Canyon lease block 36 (MC36), is at the northwest edge of a salt-cored bathymetric high in a location where seafloor exploration has revealed several hydrate outcrops (Ruppel & Amon, 2017). The video used for our analysis (Text S3b) was collected by the ROV *Deep Discoverer* (Kennedy et al., 2019) and excerpted by Ruppel and Waite (2020) in their analysis

Table 2
Site Characterization

Site	Water depth (m)	Seafloor temperature (°C)	CH_4 hydrate subcooling (°C)	CH_4 gas density (kg/m^3)	Water viscosity (μPa s)	Diffusion coefficient (cm^2/s)
Sleeping Dragon[a] (MC118)	890	5.3	5.3	76	1,490	1.84×10^{-5}
GB648	965	5.3	5.9	84	1,489	1.84×10^{-5}
Barkley Canyon[b]	985	3.6	7.8	87	1,570	1.82×10^{-5}
Horn Dome (MC36)	1,034	4.2	7.6	93	1,540	1.82×10^{-5}
Confetti[a] (GC600)	1,190	4.4	8.6	108	1,528	1.83×10^{-5}
New England Seep 2	1,418	4.2	10.2	132	1,534	1.82×10^{-5}

Note. Subcooling below the local methane hydrate stability temperature is calculated using the stability curve formulation from Tishchenko et al. (2005). Methane gas density is calculated for the seafloor pressure and temperature conditions according to the methane equation of state from Sychev et al. (1987). Water viscosity is from Lemmon et al. (2016). The diffusion coefficient is calculated based on a quadratic fit in temperature to data from Akgerman and Gainer (1972).

[a]Depth and temperature data from Wang et al. (2016). [b]Depth and temperature data from Seabrook et al. (2019).

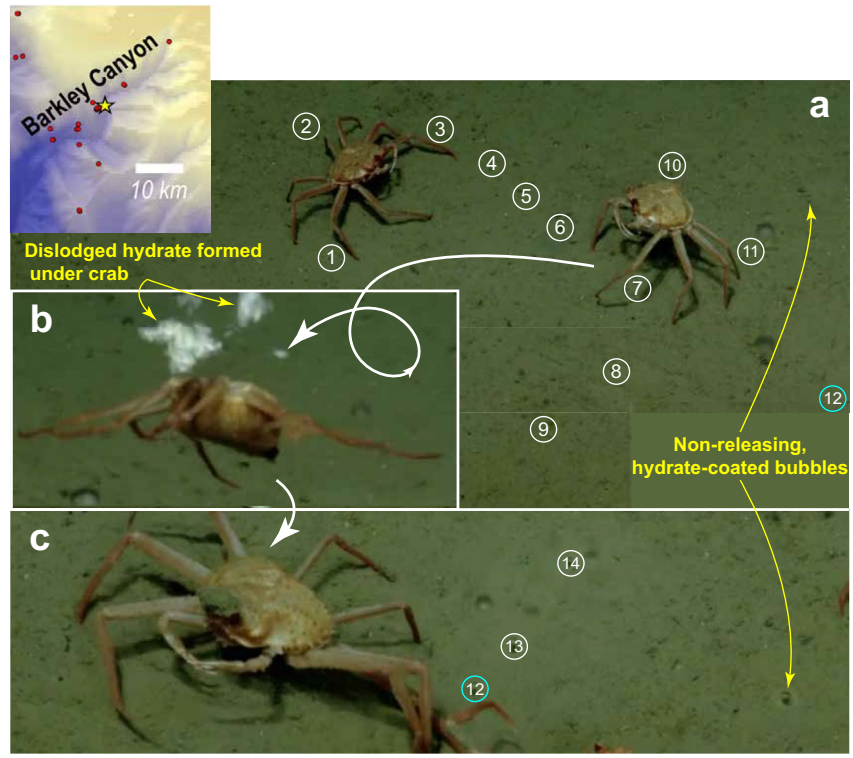

Figure 2. Inset: Map of known seeps (red) from Riedel et al. (2018) and the focus seep site (star) in Barkley Canyon, offshore Vancouver Island. (a) Seep orifices identified prior to the crab flip (see text) are indicated by circled numbers. As the tanner crabs (*Chionoecetes tanneri*) feed, seep gas collects beneath the crab on the right, eventually lifting the crab off the seafloor. (b) As the crab begins to flip, white hydrate flakes detach from the crab's underbelly. (c) After the crab lands to the right of its takeoff position, two additional emitter sites could be tracked. Note that emitter 12 (blue circle) is the same in panels (a) and (c). The rising bubbles were shiny and clear, from which we interpret they did not have hydrate coatings. Two bubbles that appeared to have gray, rigid hydrate shells and never released from the seafloor are indicated in panels (a) and (c). For scale, the flipping crab's carapace is ~7 cm across based on the ROV's laser spacing (visible in the video but located outside the area imaged here). Imagery is modified from bottom water video archived by Ocean Networks Canada and from the supplement to Seabrook et al. (2019). See Text S1 for video descriptions and links (Text S1c contains the specific clip referred here).

of seafloor hydrate phenomena. The video grab (Figure 4) shows a hydrate outcrop draped with a thin layer of fine-grained sediment. Exposed hydrate has an orange tint. Though we do not have any direct sampling from this site, previous work has shown that oil staining (Beaudoin et al., 2014; Kennicutt, 2017; Sassen et al., 2004) or perhaps bacterial crusting (Kennicutt, 2017) can give hydrate an orange coloring. In addition to the eelpouts, the outcrop hosts ice worms (Ruppel & Amon, 2017) feeding directly on the exposed hydrates and likely contributing to the formation of burrows and cavities in the hydrate itself (Fisher et al., 2000). Whereas the GB648 emitters are orifices in the fine-grained sediment, HD emitters (Figure 4b) appear directly connected to the hydrate and primarily protrude from underneath exposed hydrate. Emitter HD5 is an extreme example in which the visible hydrate shell is part of an accumulating gas pocket underneath the hydrate ledge. HD also offers a chance to peer inside certain hydrate-coated methane emitters. HD4 is the primary example of a preexisting hydrate tube from which bubbles are released at the top. The tube is transparent enough that rising menisci are visible, a phenomenon that suggests the simultaneous flow of gas and water in the subsurface environment that feeds this seep.

The Sleeping Dragon seep, which is located west of Whiting Dome in MC118, has orange-tinted hydrate covered in some places by a thin layer of fine-grained sediment (Figure 5). Similar to the HD site, the orange color could be due to oil impurities or bacterial crusting. According to the descriptions of Wang and Socolofsky (2015) and Wang et al. (2016) for the ROV *Hercules* dives in 2014, Sleeping Dragon also has hydrate tube vents. Bubbles produced by the line of individual vents made of hydrate (see *hydrate tube vents* in Figure 8) are described by Wang and Socolofsky (2015) as being primarily free of hydrate or oil films.

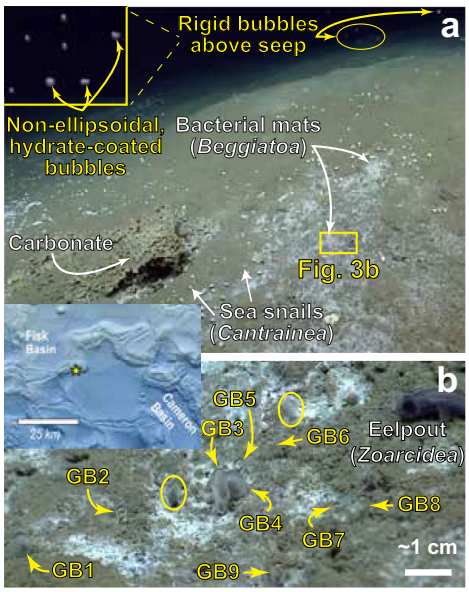

Figure 3. Inset: Location of Garden Banks seep (GB648) at the edge of a salt withdrawal basin in the northern Gulf of Mexico. (a) Overview image estimated to be ~3 m across (Text S2b). The seep is within the white bacterial mat on a mound draped in light brown, fine-grained sediment. Upper left inset shows rigid-walled bubbles imaged ~2 m above the seep (Text S2d). Bubble analysis area is highlighted in yellow. (b) Close-up: Emitter identifiers are shown for orifices with measurable bubble release rates (average release times shown in Figure 8). This site has a combination of the shiny, clear bubble surfaces associated with hydrate-free bubble surfaces (e.g., GB2, GB5, and the tops of GB6-9) and the gray or silvery surfaces associated with hydrate (e.g., GB1, GB3, and GB4, the bottom portions of GB6-9 and the circled bubbles). The two hydrate-crusted bubbles circled in yellow did not release during the ~5-min this site was imaged (Text S2b and S2c).

The Confetti seep site (Figures 1a and 6), which is located in Green Canyon (GC) 600, lies along a steep scarp bounding a salt withdrawal basin ~30 km NNW of where Green Canyon cuts into the Sigsbee Escarpment. The site was visited by ROV *Hercules* in 2014 (Wang et al., 2016). Fractured authigenic carbonate is exposed at the seafloor, and bubbles emerge primarily in a single, rapid stream from a seafloor crack. No hydrate is visible, although the site is well within the hydrate stability field (Table 2). Unlike the small bubbles released at the other sites in this study, the Confetti seep produces relatively larger bubbles that Wang et al. (2016) observe breaking up into 1–4 mm radii bubbles within the first meter of rise. These reduced size bubbles are typical of those at the other sites in our study.

3.3. United States Atlantic Margin

The final seep site examined in this study lies at ~1,400 mbsl on the heavily eroded continental slope of the New England passive margin. New England Seep 2 (Figure 7) is located on a ridge between unnamed canyons east of Shallop Canyon (McVeigh et al., 2018; Skarke et al., 2014). Similar to the Barkley Canyon site, New England Seep 2 was emitting primarily hydrate-free bubbles from fine-grained sediment and had a high concentration of red crabs, *Chaceon quinquedens* (Quattrini et al., 2015) during exploration with ROV *Deep Discoverer* in 2013. The seep site is surrounded by white bacterial mats that may also contain gas hydrate (Shank et al., 2014), and the bubble emissions are slightly slower than at Barkley Canyon. One of the slower emitters (NE1, Figure 7b) produces tubular-shaped bubbles similar to those from emitter GB3 (Figure 3), each with a clear, shiny hemispherical top and an extended lower portion that we interpret to be developing a hydrate coating as it becomes gray and opaque (see Text S6b for video link and also the supplementary videos in Skarke et al., 2014).

4. Seafloor Observations

Seafloor bubble release is characterized here according to bubble release time, hydrate coating morphology and seafloor lithology. Bubble release time is defined as the time it takes for a bubble to grow prior to being released from the seafloor. Observations suggest that bubble release time correlates with the extent and rate of hydrate film growth on the bubble surface prior to the moment of release. The hydrate coating itself also affects the final bubble shape, and hence its rise velocity (Bigalke et al., 2010) and methane loss rate (McGinnis et al., 2006; Rehder et al., 2002, 2009). The seafloor lithology controls the sediment's pore size distribution, which in turn influences the bubble size (Leifer & Culling, 2010) and hence its rise velocity (Clift et al., 1978) and initial methane content. Understanding these bubble release characteristics provides a foundation for assessing the extent to which gas hydrate formation may slow down the dissolution of methane into the water column once a bubble leaves the seafloor.

4.1. Bubble Release Rate

Figure 8 summarizes the results of analyzing the visual observations of bubble release within the hydrate stability zone at the selected study sites. The timing of our video analysis, calculated by counting individual video image frames, is based on the reported frame rate (generally 30 fps), and is discussed in Table S11 description. A key finding is that bubbles tend to accumulate more extensive hydrate coatings the longer they remain attached to the seafloor (slower release rate). The average release time for different types of hydrate coatings is site specific and reflects a localized competition between the rate at which the gas-water

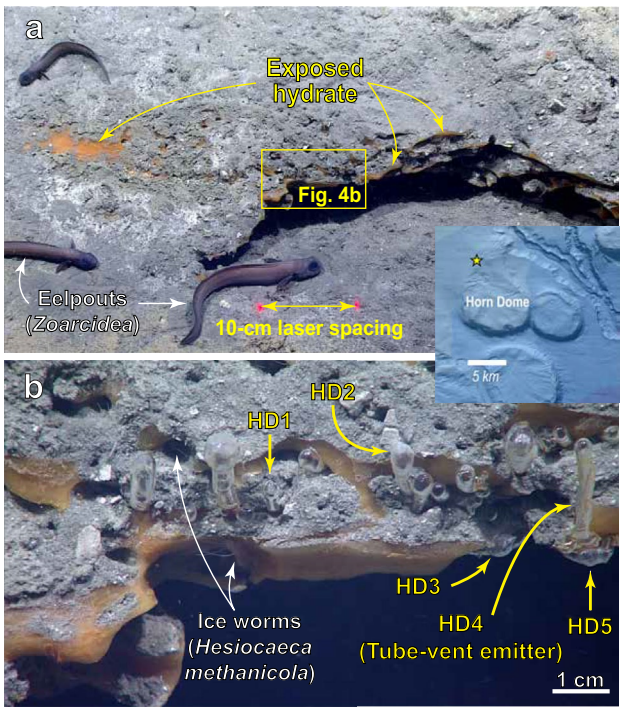

Figure 4. Inset: Location of the Horn Dome (HD) seep (MC36) northwest of the bathymetric high associated with the buried salt diapir in the northern Gulf of Mexico. (a) Overview: Bubbles form on the surface of an orange-tinted hydrate outcrop that is thinly draped with gray, fine-grained sediment. Bubble analysis area is highlighted in the yellow box. (b) Close-up: Emitter identifiers for the HD seep study area (average release times shown in Figure 8). Emitter HD5 is a gas-filled hydrate shell trapped under the hydrate ledge. Hydrate-coated bubbles not indicated by yellow arrows did not release during the 5-min video (Text S4b). Ice worms (Ruppel & Amon, 2017) identifiable by their thin, white antennae, can be seen in depressions and beneath the overhang.

interface expands and the rate at which hydrate grows on that expanding surface. This competition depends on the local methane solubility and dissolved-phase methane concentration. In general, release times for clean bubbles are less than 5 s, while forming a complete hydrate coating requires release times ~10 s or longer.

When gas flow rate is sufficiently high, the rate of bubble surface creation and freshening outpaces the rate of hydrate shell growth (Fu et al., 2020). At the Barkley Canyon site, bubble release rates are high enough that no hydrate appears to form on the growing bubbles prior to seafloor release. As the crab-flip video demonstrates (Seabrook et al., 2019), however, hydrate forms readily on gas bubbles that are collected and trapped beneath the crab (Figure 2b). Similar effects have been observed on Blake Ridge, where the local methane saturation beneath a carbonate overhang is sufficiently high to promote hydrate formation and accumulation from an underlying gas bubble source (Ruppel & Waite, 2020; Van Dover et al., 2003).

At the HD tube-vent emitter HD4 (Figure 4b), the bubble surface grows only slightly faster than the hydrate formation rate, as illustrated in Figure 9. During bubble growth, internal gas circulation (Clift et al., 1978; Pinczewski, 1981) helps shift growing hydrate films away from the emerging meniscus toward the base of the bubble (Figure 9, upper panel). Such balance between gas flow rate and hydrate growth rate, however, is delicate and can be easily disrupted by changes in gas flux (Fu et al., 2020). As discussed in Section 4.3, when the growing bubble is cut off from the tube's gas source, the bubble stops growing and the surface becomes fully hydrate-coated in less than 0.3 ± 0.03 s (Figure 9, lower panel).

It is important to note that the release time for the HD tube-vent emitter (HD4) is shorter than that of the neighboring hydrate-free bubble emitter (Figure 4b, emitter HD1). Some aspects of HD4's gas or water chemistry may differ from that of HD1, accelerating hydrate growth at HD4. This observation is a reminder that the relationship between release time and hydrate formation (Figure 8) is also extremely sensitive to localized hydrate formation conditions (methane concentration, surfactants, etc.). In general, however, bubbles with release times below 2 s rarely have hydrate coatings for the sites considered here.

Despite some variabilities, Figure 8 implies that after ~5–10 s bubbles attached to the seafloor generally become hydrate coated. We hypothesize that this timescale also serves as a good estimate for the total seawater exposure time for a bubble to become hydrate coated. The total seawater exposure time includes both the time a bubble spends attached to the seafloor (seafloor residence time) and the time of its subsequent ascent through the water column.

To elaborate on this hypothesis, we note that an initially clean bubble could become hydrate-coated during its subsequent rise. When an initially clean bubble releases from the seafloor, drag from the surrounding water on the bubble surface maintains meniscus motion from the top toward the bottom of the rising bubble (McGinnis et al., 2006; Warzinski et al., 2014), just as observed for seafloor-grown bubbles (Figure 9a). Though this can slow hydrate growth, a hydrate film nonetheless begins growing almost immediately (McGinnis et al., 2006; Rehder et al., 2009). Within the first 100–200 cm of rise within the water column, many of the bubbles visible at GB648 appear to be gray and rigid and are probably coated in hydrate (Figure 3, inset). Wang et al. (2016) indicate that all bubbles observed 150 cm above the Sleeping Dragon and Confetti seeps are definitely hydrate-coated. As discussed in Text S9, for the observed bubble diameters (3–5 mm for HD, 2–6 mm for Sleeping Dragon, and 2–10 mm for Confetti), rise velocities range from 15 to 22 cm/s, suggesting the bubbles would take ~7–10 s to rise 150 cm. This calculated time is consistent with

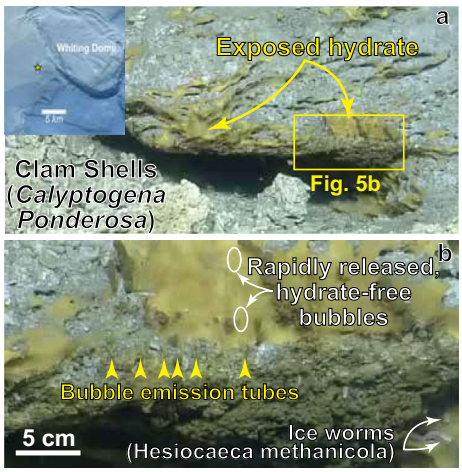

Figure 5. Inset: Location of the Sleeping Dragon (MC118) site near Whiting Dome in the northern Gulf of Mexico. (a) Overview: Orange-tinted hydrate outcrop covered with thin sediment. Broken clam shells (*Calyptogena*) are piled on the left side of the mound. (b) Close-up of the yellow box from (a), showing ice worms on the hydrate surface. A line of hydrate vent tubes, similar to those at Horn Dome (HD) emitter HD4 (Figure 4b) produce bubbles rapidly (~0.1 s per bubble or faster). Vent tubes and bubbles are more easily distinguished in the original video (Wang & Socolofsky, 2015, also Text S4b), from which this imagery is extracted.

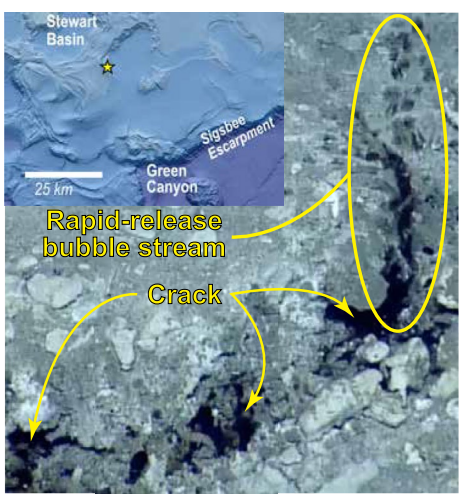

Figure 6. Confetti seep site (GC600; Figure 1a). Inset: Map showing the seep location (star) at the edge of a salt withdrawal basin in the northern Gulf of Mexico. Main image: A stream of relatively large bubbles is emitted from a seafloor crack within carbonate-dominated rock. Wang et al. (2016) note these bubbles break up within the first meter of rise. After breakup, 1–4 mm bubble radii were measured by Wang et al. (2016). The image is ~1 m across. Imagery is modified from video in the supplement to Wang et al. (2016), see also Text S5b.

the seafloor observations shown in Figure 8, where only a single one of the nine bubbles with release times longer than ~10 s is hydrate free.

Thus, for the sites described here, our analysis suggests that bubble surfaces are generally hydrate-coated within 10 s of exposure to seawater, regardless of whether the bubble is initially coated at the seafloor. This 10 s includes both the seafloor residence time and subsequent bubble rise. For instance, a bubble releasing after only 2 s would be anticipated to release as a clean, hydrate-free bubble (Figure 8), but become hydrate coated within the first 8 s of rise.

4.2. Hydrate Coating Morphology During Bubble Growth

Figure 8 indicates not only that bubble release time correlates with the extent of hydrate coverage on a bubble, but also where and how thickly that hydrate forms. Extensive hydrate growth can significantly alter both the shape and methane content of a bubble, two characteristics that in turn influence where the bubble's methane will dissolve in the water column. In general, hydrate growth begins at the base of the bubble, where the gas has been in contact with seawater the longest. As the release time increases, gas hydrate can grow farther up the sides of the bubble until only a small cap of hydrate-free bubble surface remains (Figure 8, right panel, chimney-growth bubble). Hydrate can completely cover slow-growing bubbles (Figure 8, right panel, film-coated bubbles), forming thicker, more rigid shells over time (Figure 8, right panel, shell-coated bubbles).

Pronounced hydrate shell growth significantly alters the shape of seafloor bubbles. Figure 10 shows three stages of a chimney-growth bubble. This chimney-like bubble growth shape occurs because the hydrate growth directs bubble expansion toward the surface of least resistance (Fu et al., 2018, 2020), which is generally the top of the bubble. The coupled effect of hydrate formation and bubble expansion also creates minor bends in the final bubble shape (Figure 10 here, and also Figure 4 in Fu et al., 2018). These rigid, non-spherical, large aspect ratio (width/height) shapes have been observed to yield reduced rise velocity in hydrate-coated bubbles (Bigalke et al., 2010).

Numerous fully coated bubbles are observed (e.g., Figures 3 and 4b) when the bubble release time becomes sufficiently long. Though direct thickness measurements are not possible, we assume that the apparent elasticity of the coating correlates with the shell thickness. Thus, a shell that is more easily stretched is assumed to be thinner than a more rigid one. HD emitter HD2 (Figure 4b) produces thinly coated bubbles, which act like inflating balloons (Figure 11a). These pliable, thin-shelled bubbles have 38 s average release times. HD emitter HD3 produces more rigid bubbles that grow via cracking, stepwise expansion, and rapid crack healing (Figure 11b), with an average release time of 33 s. In comparison, two rigid, opaque, potentially thicker-shelled bubbles from GB648 (emitters GB1 and GB4, Figure 3b) each release only once during the video. Their minimum possible release times are 41 and ~170 s, respectively. HD has several hydrate-coated bubbles that do not release during the 5-min video (e.g., the two larger tubes to the left of HD1in Figure 4b). These bubbles appear to have thicker shells than those that do release.

An important consequence of these diverse hydrate-coating processes is the emission of irregularly shaped bubbles into the water column

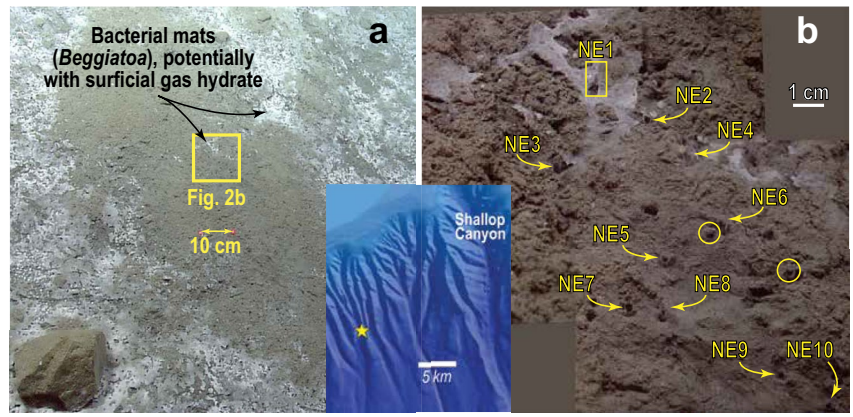

Figure 7. Inset: location of New England Seep two on the continental slope south of Massachusetts. (a) Overview image showing bubble release primarily within the tan patch of bare seafloor surrounded by white bacterial mats. Bubble analysis area is highlighted in yellow. (b) Emitter identifiers for the New England Seep 2 (NE) seep study area. Yellow circles indicate bubbles that remain fixed at the seafloor during the entire ~2 min of video for this site. The two yellow circles mark bubbles that remain fixed to the seafloor during the video. These stationary bubbles appear less reflective than the neighboring bubbles from emitters 5, 8, and 9, suggesting they may be coated by thin hydrate shells. The video can be accessed in Text S6b.

(Figures 10 and 11, right-hand panels). As noted in Section 4.1, many of the bubbles observed 150–200 cm above the seafloor at GB648 are hydrate coated, rigid, and irregularly shaped. Wang et al. (2016) makes the same observation above the Sleeping Dragon and Confetti sites (see Figure 6 in Wang et al., 2016). This suggests that, at seep sites where hydrate coating occurs, bubble plumes likely consist of a combination of irregularly shaped and rigid shelled bubbles as well as clean bubbles. The hydrodynamic interactions within these shelled-bubble swarms may differ significantly from that of hydrate-free bubbles and influence plume dissolution dynamics.

4.3. Lithology and Bubble Release Controls on Bubble Size

Lithologic control on the size of bubbles released at the seafloor has been examined by Leifer and Culling (2010), who classify seep lithologies according to the sediment grain size relative to the bubble size. For fine-grained lithologies in which bubble radii are much larger than sediment grain radii (e.g., Barkley Canyon and GB648), Leifer and Culling (2010) note that gas can become temporarily trapped and accumulate below the seafloor before being released in a pulsed mode capable of lifting and mobilizing the sediment grains. The Leifer and Culling (2010) study utilizes non-cohesive grains without pre-existing flow paths, however. Though sediment motion in response to bubble release can be seen in the video (e.g., at NE7 in Figure 7b), the generally steady, non-pulsing bubble releases at Barkley Canyon, GB648, and New England Seep 2 suggest the fine-grained sediments at these sites are sufficiently cohesive and the seeps are mature enough to have developed a subsurface network of unobstructed gas pathways and emission points. Such a near-surface network is likely connected to a larger, dendritic subsurface conduit system, as imaged in 3D beneath the Blake Ridge seep field (Hornbach et al., 2007).

For unobstructed emission at the seafloor-water-column interface, a capillary tube is a good analog for the shape of an emitter's pore structure (Leifer & Culling, 2010). Here we assume that seafloor bubbles are released from a capillary tube-like structure with a circular orifice. The typical bubble size should then reflect a balance between gas buoyancy and gas/water surface tension at the orifice. For hydrate-coated bubbles, the tensile strength of hydrate coating can enhance the gas/water surface tension, potentially allowing larger bubbles to form. Here we test this hypothesis by calculating the theoretical bubble size under hydrate-enhanced surface tension and compare our calculations to field observations.

Assuming a circular orifice, Davidson and Amick (1956) and Oguz and Prosperetti (1993) demonstrate that the maximum volume of a clean bubble, V_{max}, at the moment of release should be determined by the balance between the bubble's buoyancy and the surface tension at the orifice:

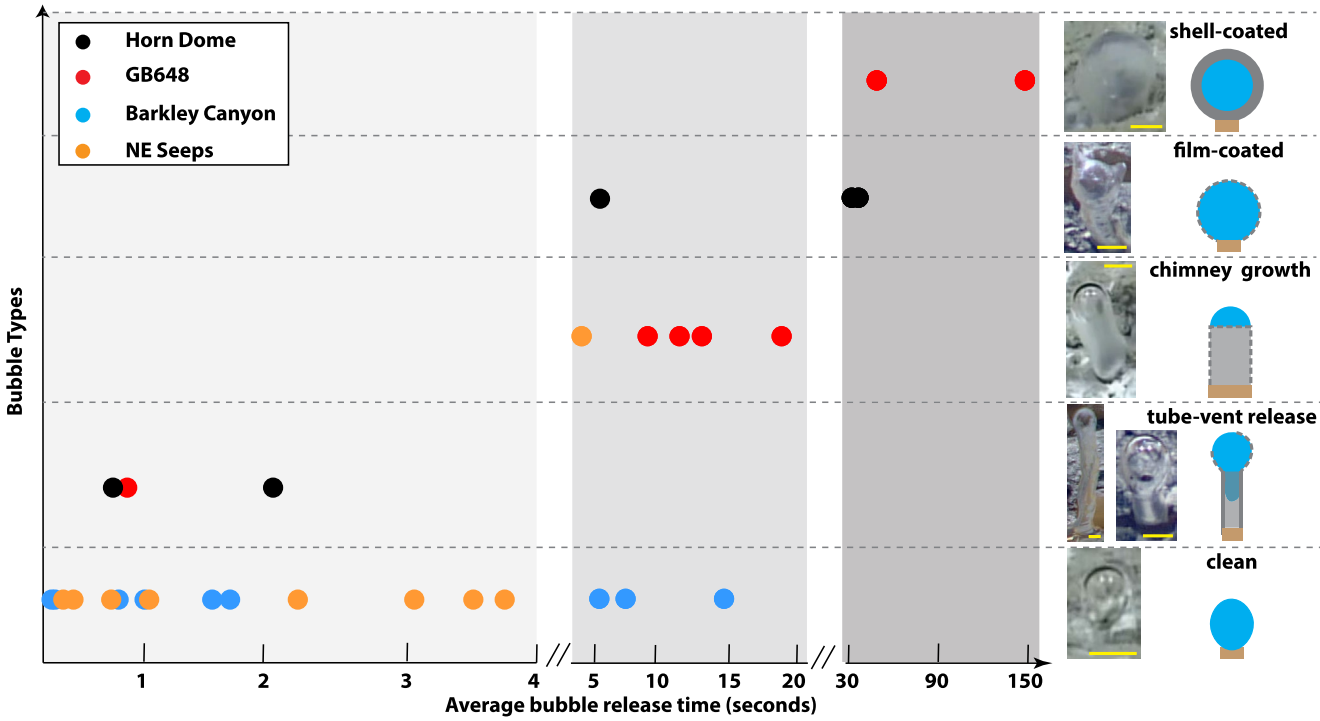

Figure 8. Relationship between bubble release time and type of bubble released. Release times for the clean bubbles at Sleeping Dragon could not be precisely determined but are estimated to be 0.1 s or less (not plotted). Example snapshots from Horn Dome and GB648 are shown on the right (yellow scale bars = 2 mm), along with schematic diagrams of gas (blue), hydrate (gray), and ground (brown) to illustrate various bubble types and their growth processes. In these schematic diagrams, solid gray lines represent pre-existing hydrate that remains unchanged from bubble to bubble; dashed gray lines represent hydrate films that can grow along with the bubble, progressively coating the gas/water interface. Longer release times generally correlate with more hydrate coverage of the meniscus and thicker hydrate walls/shells, but the precise release-time transitions between different shell morphologies will depend on the local solubility and dissolved-methane concentration conditions. The tube release schematic illustrates a potential internal fluid meniscus-based mechanism for controlling bubble release (see also Figure 13). NE seeps corresponds to New England Seep 2, offshore Massachusetts.

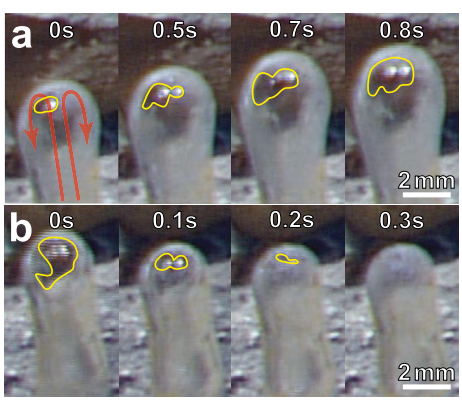

Figure 9. Bubble growth rate relative to hydrate film growth rate for the Horn Dome (HD) tube-vent emitter (HD4, Figure 4b). (a) Time series showing active bubble growth producing a gas/water meniscus (outlined in yellow). Internal gas circulation (red arrows at time 0 s; Clift et al., 1978; Pinczewski, 1981), helps shift the growing hydrate film (gray regions surrounding yellow outline) away from the active meniscus growth. (b) When flow is shut off to this emitter, the gas/water meniscus (outlined in yellow) is rapidly coated in hydrate (<0.3 s).

$$V_{\max} = \frac{2\pi \cdot r_{\text{orifice}} \cdot \sigma}{\left(\rho_w - \rho_g\right) \cdot g}, \quad (1)$$

where r_{orifice} is the emission orifice radius (m), σ denotes the bubble's surface tension (taken to be 0.061 N/m for methane at the water depths in this study (Sachs & Meyn, 1995)), ρ_w represents the seawater density of 1,030 kg/m^3 (Fofonoff, 1985), ρ_g is the methane gas density (Table 2), and g gives the gravitational acceleration of 9.807 m/s^2. Davidson and Amick (1956) note that bubbles can grow up to $2V_{\max}$ for the low flow rates observed in this study (Text S7). By analogy to Equation 1, the maximum volume, $V_{\text{max, hydrate}}$ of a bubble held to the orifice by the tensile strength, τ, of a hydrate film of thickness, δ, is given by:

$$V_{\text{max,hydrate}} = \frac{2\pi \cdot r_{\text{orifice}} \cdot \tau \cdot \delta}{\left(\rho_w - \rho_g\right) \cdot g}. \quad (2)$$

Jung and Santamarina (2011) measured the tensile strength for methane hydrate to be 0.2 MPa. The initial film thickness of methane hydrate forming on a gas/water interface is ~10 μm (Li et al., 2017; Yin et al., 2018). To obtain a conservative volume estimate of $V_{\text{max, hydrate}}$ bubble size, we will assume only a 1 μm shell thickness.

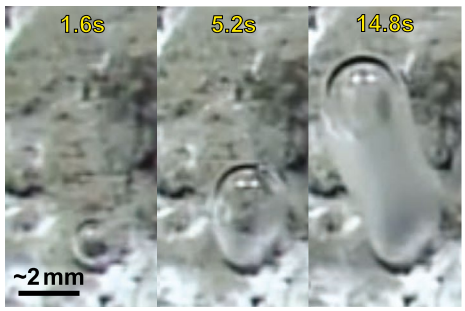

Figure 10. Chimney-type bubble growth. GB648 emitter GB3 initially grows spherically, with a shiny, hydrate-free interface (left panel). Hydrate film growth (gray, frosty coating at the bubble's base in the middle panel) deflects the subsequent bubble growth to the left, coating the sides of the bubble as the bubble grows (middle and right panel). The top of the bubble is still a hydrate-free meniscus because the bubble growth rate nearly matches the pace of hydrate film growth, unlike the case in Figure 9b. The right panel image is taken 1/60th of a second prior to the entire chimney-bubble's release. This bottom-up hydrate growth pattern has also been observed on laboratory-formed bubbles (Li et al., 2017).

We compare the theoretical predictions with measured bubble volumes from the seafloor videos. Figure 12a shows the volumes of bubbles released from the two most active orifice-based emitters relative to the predicted V_{max} based on Equation 1 (HD1, $r_{orifice}$ = 0.6 mm, V_{max} = 27 mm^3, and HD4, $r_{orifice}$ = 1.3 mm, V_{max} = 53 mm^3) at HD. Nearly all bubbles are smaller than V_{max}, and none exceed $2V_{max}$. By comparison, even for the smaller emitter HD1, a 1 μm hydrate shell is strong enough to balance the buoyancy force of a bubble of $V_{max, hydrate}$ = 87 mm^3, which is much larger than the bubbles observed at HD and GB648.

A key uncertainty in the bubble size calculation is the value of gas/water surface tension (σ) at a given temperature. As shown in Equation 1, the maximum bubble volume scales linearly with surface tension. Consequently, methane bubbles forming at ambient, room temperature conditions (σ = 0.072 N/m, Sachs & Meyn, 1995) could reach volumes 18% larger than when forming at the bottom water conditions for HD (σ = 0.061 N/m, Sachs & Meyn, 1995). In the GOM, the coexistence of higher hydrocarbons (e.g., ethane and propane) in the bubble decreases the surface tension relative to the pure methane gas phase results (Hayama et al., 2017), as does the presence of oils (Hollebone, 2011). A mixture of 90.06 mol% methane, 6.8 mol% ethane, and 2.6 mol% propane at 10 MPa (close to the 10.4 MPa at HD, and nearly identical to the 90/7/3 mol% mixture discussed in Section 5.1 and by Sloan & Koh, 2007) has σ = 0.051 N/m (Hayama et al., 2017). The presence of oils, by comparison, will typically reduce the surface tension to ~0.018–0.032 N/m depending on the oil. To get a sense of the lower bound on V_{max}, we can consider the water to instead be the crude oil studied by Soloviev et al. (2016), with σ = 0.028. In this hypothetical case, V_{max} could be as small as 12 and 24 mm^3 for HD1 and HD4, respectively.

We do not expect oil to be a controlling factor for the hydrate-coated bubble sizes because of the dependence of $V_{max, hydrate}$ on the hydrate tensile strength (Equation 2) rather than the surface tension (Equation 1). However, a mixed gas system of 90/7/3 wt% methane, ethane and propane could have an effect because such a mixture will form structure II (sII) hydrate rather than the structure I (sI) hydrate formed by pure methane. Jung and Santamarina (2011) measured the sII hydrate tensile strength to be at least 0.16 MPa, meaning bubbles at least as large as 70 mm^3 could form at HD emitter HD1. While this is less than the predicted $V_{max, hydrate}$ = 87 mm^3 for sI methane hydrate, the bubble volume predicted by Equation 2 is still much larger than the observed bubble volumes. We therefore conclude that the presence of hydrate coating, which is expected to increase the effective surface tension at the point of release, is not systematically increasing bubble sizes at these sites. It may be that imperfections in the hydrate coating at the gas/water interface near the orifice allow direct contact between gas and water at the orifice, significantly reducing the effective tensile force that anchors down the bubble against its buoyancy. Nevertheless, the data suggest that hydrate film growth increases bubble volume variability, where hydrate-coated bubbles are significantly more variable in their sizes compared to the hydrate-free bubbles (Figure 12b).

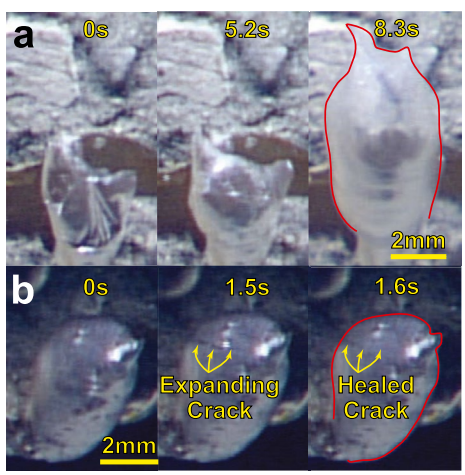

Figure 11. Bubble growth with no free-gas interface. (a) Horn Dome (HD) emitter HD2 (Figure 4b) has a hydrate shell thin enough to deform as gas is introduced from below. (b) HD3 (Figure 4b) expands via cracking (middle panel) and crack healing (right panel) that is too rapid for free gas to escape. This crack-healing formation process has been observed in laboratory studies, also with no free gas release (Li et al., 2014). In both panels (a) and (b), the final bubble forms have irregularities and protrusions highlighted by red outlines in the last panels. These protrusions will increase drag and reduce the bubble rise rates.

Hydrate also contributes to the lithologic framework of seeps. HD and Sleeping Dragon are both hydrate outcrops with thin sediment drapes (Figures 4 and 5 above, and supplemental videos in Wang & Socolofsky, 2015; Wang et al., 2016). Most of the bubble emissions come from areas of exposed hydrate. The rigid hydrate appears to promote capillary tube-type emissions sites (e.g., emitters HD1 and HD4 in Figure 4b and the emitters in Figure 5b), and also provides a ledge underneath which gas can accumulate.

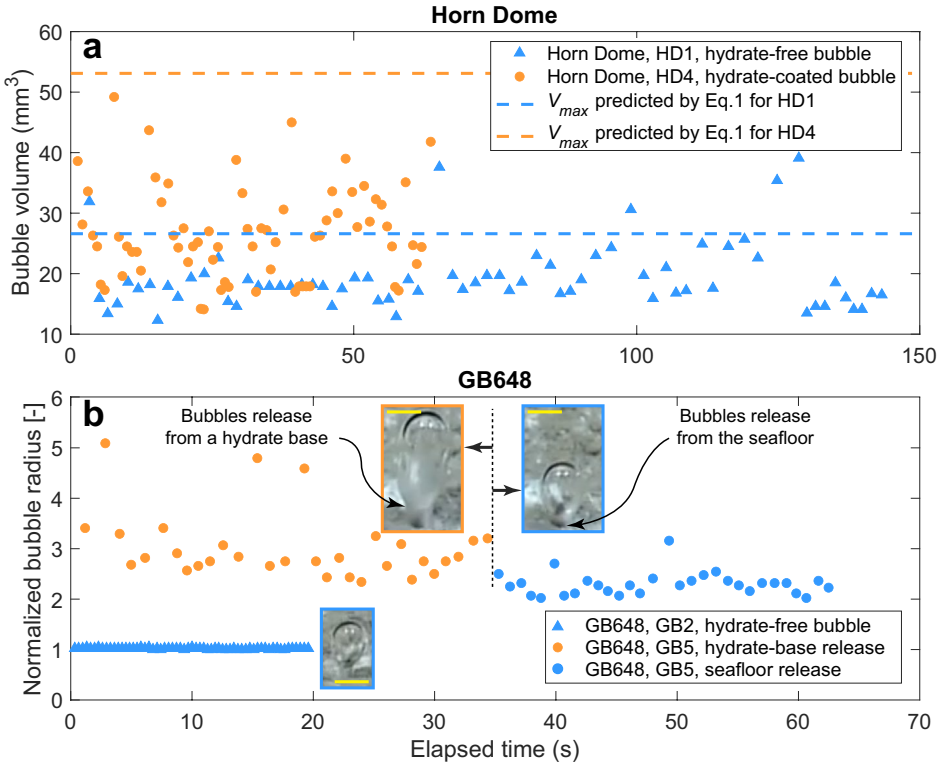

Figure 12. Gas hydrate film influence on bubble size and variability. (a) At Horn Dome, bubbles growing with concurrent growth of a hydrate film (orange circles) are larger and more variable in volume than the hydrate-free bubbles (blue triangles). Maximum bubble sizes are comparable with V_{max} predicted by Equation 1 (dashed lines). (b) At GB648, sizes are normalized by the average release diameter for emitter GB2 (blue symbols) because no length scale was available during that observation period. Yellow scale bars in insets are ~2 mm. Emitter GB2 produces clean bubbles (blue triangles). Emitter GB5 initially produces bubbles with a normalized diameter range (2.9 ± 0.6) from a conical hydrate base (orange symbols). The cone detaches during the bubble release at ~34 s, after which bubbles grow primarily from the ground with minimal hydrate coating. The clean bubbles emitted at GB5 (blue circle) are slightly smaller and with less variability, with size estimated to be 2.2 ± 0.2. The time axes correspond to the video interval lengths we used to document the behavior of each emitter. In panel (b), 61 bubbles were released from each emitter. This took just under 20 s at GB2 (average release rate = 0.32 s/bubble), and just over 62 s for GB5 (average release rate = 1.02 s/bubble).

The subsurface plumbing is generally difficult to probe at the spatial scale relevant for bubble generation, but the tube-vent emitter HD4 (Figure 4) provides a rare opportunity to visualize how subsurface fluid and gas co-flow to generate bubbles. As shown in Figure 13, the tube-vent emitter walls are transparent enough to view the motion of fluid/gas menisci within the emitter, indicating that its fluid source is a mixture of gas and water. Gas/fluid menisci can enter the tube and rise to the top, triggering a bubble release (Figure 13, top row). In this case, the bubble size is not determined by the tube radius; instead, it reflects the size of the gas slug partitioned by the subsurface pore network. Figure 13a (right panel, tube-vent release) illustrates this release mechanism, in which the rising meniscus indicates the bottom of the gas slug. Regardless of its size, the gas slug releases when its trailing meniscus rises to the top of the tube. Subsurface pores are often heterogeneous in size, generating gas slugs of various sizes and contributing to the variability in measured bubble volumes from this type of emitter (Figure 12a). The yellowed coloring of the rising meniscus indicates the presence of oil, which, as discussed in Section 4.3, will reduce the surface tension relative to a purely gas/water system and thereby facilitate the release of the bubble.

Internal menisci can also develop a rigid hydrate coating and suddenly shut down an emission site. As shown in Figure 13b, meniscus #2 develops a hydrate skin within the tube vent, diverting flow from the upper emission site to a new site at the base of the tube (emitter HD5). The bubble forming at the upper emission site, under reduced gas flow, rapidly forms a hydrate crust (crust formation shown in Figure 9b).

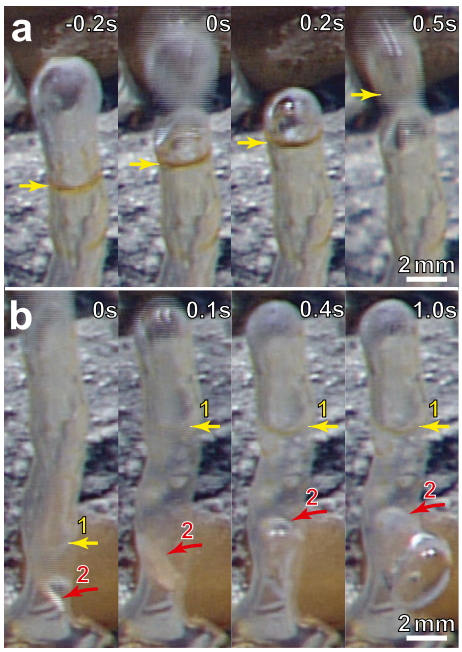

Figure 13. Internal meniscus control on bubble release in Horn Dome (HD) tube-vent emitter HD4 (Figure 4b) can be visualized (arrows) because the tube is nearly transparent. (a) After the previous bubble release (second panel, 0 s), the rising meniscus reaches the top of the tube and releases the bubble in only 0.5 s. The average release time for this emitter is 0.9 ± 0.3 s. Internal menisci control on bubble release can add variability to the average release time. (b) Two internal menisci (yellow and red arrows) split, potentially due to fluid invasion from outside the tube. The upper meniscus becomes stationary, blocking flow to the top of the emitter (see Figure 9b). The lower meniscus also becomes blocked, frosting over with hydrate (between panels 3 and 4) and diverting flow out the side of the tube (panel 4, 1.0 s). A thin ring of silvery hydrate can be seen where the new bubble contacts the tube. The new bubble grows in the chimney-type pattern illustrated in Figure 10 before releasing.

The tube section between the highlighted interfaces in Figure 13b is filled with liquid water rather than gas. The entire tube breaks away from the seafloor (at the 3:39 min mark in the HD video accessible from the link in Text S3b). An internal water-filled section would significantly reduce the tube's buoyancy. With low buoyancy and its irregular shape, the tube would be anticipated to rise more slowly than a hydrate-free bubble of equivalent total volume. Our inability to observe the subsurface gas flow precludes any attempts to generalize this type of emitter behavior to other emission sites, but we speculate that subsurface-controlled bubble generation could occur elsewhere.

4.4. Gas Flux Variability Within a Single Seep Site

The seafloor videos analyzed in this study also provide a rare opportunity to quantify gas fluxes at high spatial resolution, where the flux from each emitter can be individually estimated. Here, we calculate gas flux from a selection of individual emitters as release rate (bubbles/s) multiplied by average bubble volume (mm^3). We perform this calculation for New England Seep 2 (Figure 7) and summarize the results in Table 3. Emitters are chosen to examine flux differences due to orifice size, release rate and bubble size. We find that, within the same seep field, the estimated gas fluxes from individual emitters can differ by a factor of up to 6, though there is an overall trend of increasing flux toward the downslope portion of the seep (toward the lower right in Figure 7b). Here, we use Darcy's law to provide a theoretical understanding of what contributes to the variability in gas flux observed amongst individual emitters. According to Darcy's law, the gas flux, Q, through an emitter orifice of area $\pi \cdot r^2_{\text{orifice}}$, should depend on the permeability of the underlying gas conduit, k, the pressure gradient driving flow, $\Delta P/L$, and gas viscosity μ:

$$Q = \frac{\pi \cdot r^2_{\text{orifice}} k \Delta P}{\mu \cdot L}. \quad (3)$$

While the individual bubble size is determined by the orifice size of an emitter (Equation 1), the overall gas flux at an emitter (average bubble volume multiplied by release rate) is determined by the flow through its underlying conduit as prescribed by Equation 3. If we assume a single gas source feeds all emitters, the general trend of increasing flux downslope could be explained by an increasing pressure gradient ($\Delta P/L$)

Table 3
Characteristics of Bubble Release at a Selection of Emitters Within the New England Seep 2 Site

Emitter number	Orifice radius (mm)	Release time (s/bubble)	Release rate (bubbles/s)	Bubble volume (mm^3)	Theoretical V_{max} (Equation 1) (mm^3)	Gas flux (mm^3/s)
1[a]	1 ± 0.2	4.3 ± 1.4	0.3 ± 0.2	35 ± 13	44	8.2 ± 0.8
2[a]	1 ± 0.2	1.2 ± 0.4	0.9 ± 0.2	26 ± 9	44	21 ± 2
6	1 ± 0.2	0.9 ± 0.2	1.1 ± 0.2	33 ± 6	44	35 ± 2
9	0.75 ± 0.2	0.5 ± 0.1	1.9 ± 0.3	25 ± 5	33	45 ± 3
10	0.5 ± 0.2	0.2 ± 0.03	5 ± 1	10 ± 2	22	46 ± 5

Note. Five emitters are analyzed (emitter numbers and substrate are illustrated in Figure 7b). We calculate the theoretical maximum bubble volume, V_{max}, using the estimated orifice radii and Equation 1. In agreement with observations at Horn Dome (Figure 12a), Vmax exceeds the measured bubble volumes. Gas flux is estimated as release rate multiplied by bubble volume.

[a]Emitters 1 and 2 contact the bacterial mat, in which hydrate may also be present (Figure 7b).

due to the decreasing conduit length (L) downslope. This line of reasoning could explain why neighboring emitters (such as 9 and 10, separated by ~2 cm but with different orifice sizes) have equivalent fluxes in spite of their differing release rates and bubble sizes (Table 3). Conversely, emitters 1, 2, and 6, all have equivalent $r_{orifice} \approx 1$ mm and thus similar bubble volumes (within the bounds of uncertainty as calculated by Equation 1); however, these three emitters have different gas fluxes and the increasing flux corresponds to the downslope direction (Table 3).

Unfortunately, we are not able to conclusively decouple potential surface controls on the flow rate and bubble size, such as the presence of the bacterial mat or gas hydrate at emitters 1 and 2 (Figure 7b), from subsurface controls, such as variations in conduit length, permeability, and/or gas sources with different pressures. The observed bubble emissions are consistent with a single gas-source system for this section of New England Seep 2, but a multi-source system is also possible.

5. Implications

Bubble release processes from seafloor within the hydrate stability zone are diverse, generating hydrate-free bubbles from rapid emission sites, and partially- to fully-hydrate-coated bubbles from sites with longer release times. By the time bubbles have risen ~150 cm off the seafloor, however, most have become hydrate-coated (Figure 3a above; Wang et al., 2016). To calculate the water-column methane dissolution profile, models have used one of two endmembers to represent the bubble's condition at the moment of seafloor release: initially hydrate-free or "clean" (Li & Huang, 2016; McGinnis et al., 2006; Topham, 1984b; Yapa et al., 2010) or initially hydrate-coated (McGinnis et al., 2006). Here we show that bubbles released with hydrate shells have ~5% more methane after their initial 150 cm rise than an initially clean bubble of the same initial volume. This difference is caused by two processes: (a) the impact of hydrate shell formation on a bubble's initial methane content and (b) the shielding effect of hydrate coating on slowing methane dissolution from a bubble. Modeling details are summarized here, with more detailed derivations provided in Text S8–S10.

These calculations are performed for different bubble radii for the four GOM sites listed in Tables 1 and 2, as well as for different water depths (seafloor depth). In generalizing to a range of water depths, we follow the approach of Frye (2008) and use the Milkov and Sassen (2001) correlation between GOM water depth, wd (m), and seafloor temperature, T (°C):

$$T = 295.1 \cdot wd^{-0.6}. \quad (4)$$

5.1. Hydrate Shell Contribution to a Bubble's Methane Content

In most environmental conditions, methane is packed at different densities (moles CH_4/cm^3) in the gas and hydrate phase (Sloan & Koh, 2007). To determine the impact of hydrate shell formation on a bubble's total methane content, we calculate the independent control of pressure and temperature on the methane gas-phase density (Sychev et al., 1987; Weast, 1987) and the methane hydrate-phase density (see Helgerud et al., 2009; Text S8). Methane density in the hydrate phase also depends on the mole fraction of methane in hydrate, taken from Fu et al. (2019) to be 0.1418 (stoichiometric ratio = $CH_4 \cdot 6.05H_2O$) as an average for the bottom water conditions given in Table 2.

The shell thickness also depends on ambient conditions such as subcooling and flow. For methane hydrate, Taylor et al. (2007) derive an empirical fit for the dependence of hydrate film thickness, δ (μm), on subcooling (Table 2), ΔT (°C):

$$\delta = 0.0887\,\Delta T^2 + 6.2585\,\Delta T + 0.0392. \quad (5)$$

This equation assumes the hydrate shell grows under quiescent conditions within 1–2 h. We use Equation 5 as the "static" endmember for shell thickness. For the GOM sites (Table 2), δ ranges between 35 and 60 μm. In the presence of ambient flow and under shorter time scales, the shell thickness is reduced (Abe et al., 2007; Liu et al., 2019). Here, we follow the approach of Li et al. (2013, 2014) and Yin et al. (2018) and consider 10 μm to be the initial, or "dynamic" endmember shell thickness.

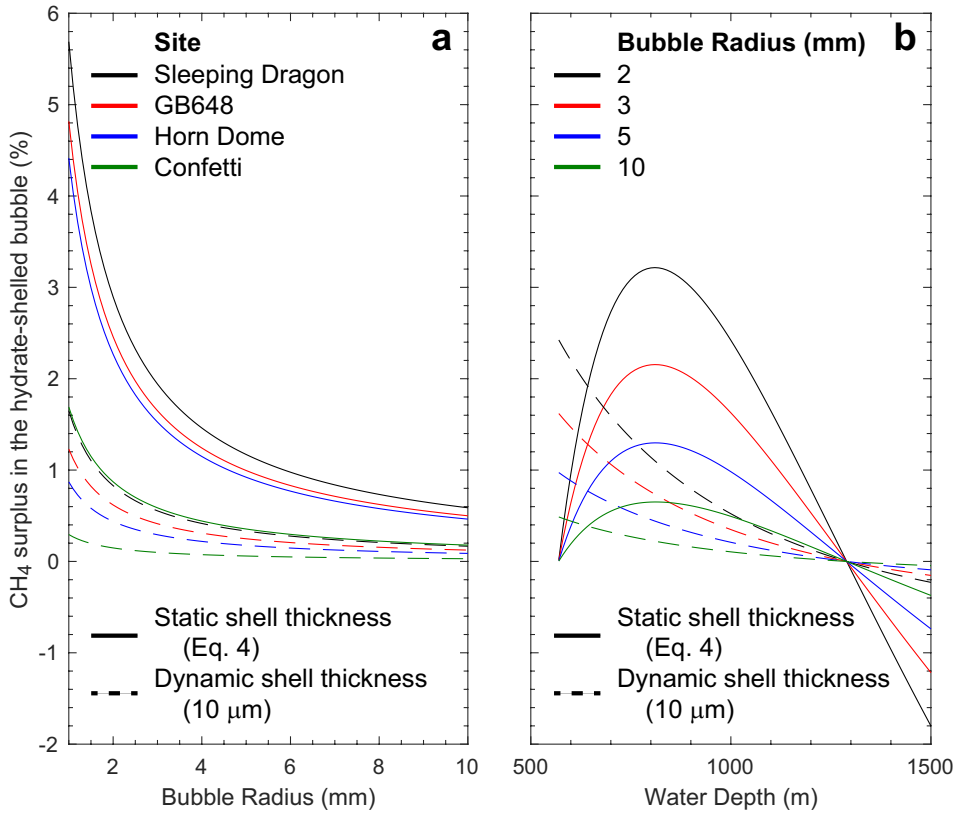

Figure 14. Methane surplus at the moment of seafloor release for an initially hydrate-shelled, spherical bubble relative to a hydrate-free bubble of equal volume. (a) Surplus dependence on bubble radius and shell thickness for the four GOM sites listed in Tables 1 and 2. (b) Surplus dependence on water depth, assuming the temperature correlation with water depth from Milkov and Sassen (2001) for the GOM. For the typical bubble radii at the sites in this study (1–5 mm), initial methane surpluses on the order of 1% can be expected for bubbles released with a methane shell relative to hydrate-free bubbles. For water deeper than ~1,300 m, however, methane is more densely packed in the gas phase than in hydrate and hydrate-shelled bubbles initially have less methane than their hydrate-free counterparts.

Figure 14 shows the percentage difference in initial methane content between a hydrate-coated and a hydrate-free bubble at the moment of seafloor release. The analysis is done for bubbles of various radii and for a range of water depths. Note that here the volume and the methane content of a hydrate-shelled bubble includes the contribution from the shell as well as the bubble's gaseous methane. Our calculation suggests that hydrate-shelled bubbles can have several percent more methane than their hydrate-free counterparts for the GOM sites considered in this study. Fundamentally, the additional methane carried by hydrate-shelled bubbles is due to methane being more densely packed in the hydrate shell than in the gaseous phase. At the pressure and temperature reported for HD (10.44 MPa, 4.2°C), the methane density is 27% higher in the hydrate phase than in the gaseous phase. As bubble radius, r (mm), increases (Figure 14a), the shell's contribution to the bubble's overall methane content decreases due to a less favorable volume-to-surface ratio, because the bubble's volume (gaseous methane contribution) increases as r^3, whereas the bubble's surface area (hydrate shell contribution) increases only as r^2.

The dependence on water depth illustrated in Figure 14b shows a crossover behavior when we assume a static shell formation (Equation 5). At shallow depths, pressure and temperature conditions approach the hydrate phase stability boundary. The subcooling and thus the shell thickness approach zero (Equation 5), and the shell does not contribute to the bubble's methane content (percent surplus is 0 at 570 m). As the water depth increases, the subcooling and shell thickness increase, but so do the pressure and gas density. As a result, in deep enough water, a hydrate-free bubble contains more methane than its hydrate-coated counterpart (Boswell et al., 2010). For the seafloor temperature assumed here, the crossover for which

methane is more densely packed in the gas phase rather than in hydrate (Lei et al., 2019; Paull et al., 2000) occurs near 1,300 m water depth.

We do not see such crossover behavior when our calculation assumes a dynamic shell formation process because we use a constant thickness of 10 μm for the dynamic case. In this case, the methane surplus in a hydrate-shelled bubble decreases monotonically with depth as methane becomes denser in the gas phase. For the r = 1–5 mm bubbles typical of this study, bubbles with hydrate shells would initially have ~1%–2% more methane than hydrate-free bubbles.

Figure 14 assumes that bubbles form from pure methane and that the hydrate shell is sI methane hydrate. If bubbles form from a mixed gas, the gas surplus is further complicated by gas fractionation occurring during hydrate formation. As an example, the mixture of 90 mol% methane, 7 mol% ethane, and 3 mol% propane (e.g., gas mixture taken from 5.2b in Sloan & Koh, 2007 and also adopted in Section 4.3) at the bottom water conditions at HD (10.4 MPa, 4.2°C) would form an sII hydrate (Sloan & Koh, 2007). The methane density in the sII shell would be 29% lower than in the gas phase; this is drastically different from the scenario of pure methane forming sI hydrate, where methane density in the hydrate shell is 27% higher than in the gas phase (Figure 14). Ethane would be similarly distributed, packed 28% less densely in the hydrate phase than in the gas, but propane would be significantly enriched (by 1,382%) in the hydrate phase relative to the gas. These density percentages are specific to the assumed gas mixture and bottom-water conditions. In general, the presence of higher hydrocarbons will result in sII hydrate formation that stores methane and ethane less densely and propane more densely than in the gas phase.

5.2. Methane Loss During the Initial 150 cm Bubble Rise

We calculate methane loss for both hydrate-free and hydrate-shelled bubbles, again assuming an oil-free, pure methane system. We consider hydrate-free bubbles to be "clean," a designation indicating the bubble surface is fully mobile, which increases the bubble's rise velocity and mass transfer rates relative to those bubbles with contaminated, coated or rigid surfaces (Clift et al., 1978). Both calculations are based on the assumption that rising bubbles dissolve via diffusion, losing methane to the water column as they ascend. The gas transfer rate was derived for a stationary bubble by Epstein and Plesset (1950). Wüest et al. (1992) and others have extended the theory to rising bubbles to establish the commonly used expression for a bubble's mass loss as a function of rise height, z (cm), as implemented by numerous studies (Leifer & Patro, 2002; McGinnis et al., 2006; Olsen et al., 2017, 2019; Rehder et al., 2009):

$$\frac{dM}{dz} = \frac{-\left(4\pi r^2\right) \cdot K \cdot \left(C_S - C_0\right)}{v}. \tag{6}$$

In Equation 6, dM/dz (moles/cm) is the change in the bubble's methane content over the rise interval dz. Given a bubble's rise velocity, v (cm/s), diffusion occurs through the spherical bubble's surface (area = $4\pi r^2$ [cm^2]), with a mass transfer rate K (cm/s). As shown in Text S9, K depends on the bubble size and rise velocity. In this study, we calculate two mass transfer coefficients $K_{\text{hydrate-free}}$ and K_{hydrate} for K in Equation 6. We adopt the McGinnis et al. (2006) approach for clean, hydrate-free bubbles by taking $K_{\text{hydrate-free}}$ from the work of Zheng and Yapa (2002). For fully hydrate-coated bubbles, we adopt a reduced mass transfer coefficient, $K_{\text{hydrate}} = 0.2 \cdot K_{\text{hydrate-free}}$, to approximate methane loss rate as suggested by observations from McGinnis et al. (2006 see also Text S9).

Diffusion across the bubble-water interface is driven by the difference between the methane solubility, C_S (moles CH_4/cm^3), and the local dissolved methane concentration, C_0 (moles CH_4/cm^3). In this study, we iteratively solve Equation 6 at 0.1 cm increments in z to calculate the methane loss over the 150 cm rise from the seafloor (Text S9). We use the equations of Duan et al. (1992) and Duan and Mao (2006) to determine C_S, which assumes no hydrate is present. Note that the presence of hydrate would reduce methane solubility (Collett et al., 2009; Zatsepina & Buffett, 1997); therefore, our assumption here overestimates C_S for hydrate-shelled bubbles. To constrain C_0, we fit measured methane concentrations from seep sites in the hydrate stability zone (Garcia-Tigreros et al., 2021; Lapham et al., 2013; Thomsen et al., 2012), as a function of height, z, from the seafloor (up to z = 10,000 cm or 100 m from the seafloor, see Text S10):

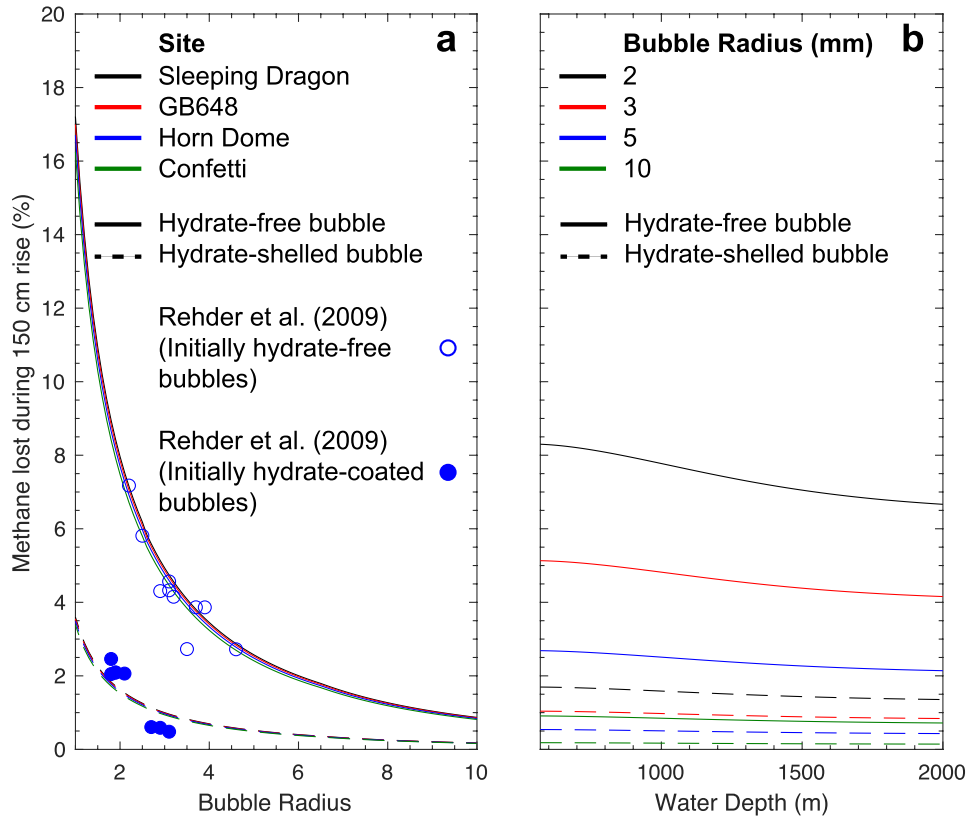

Figure 15. Percentage of methane lost via dissolution during a bubble's 150-cm rise from the seafloor for the Gulf of Mexico (GOM) seep sites. (a) Dependence on bubble radius for the four sites listed in Tables 1 and 2. Solid lines are calculated from Equation 6 for hydrate-free bubbles as described in detail in the Text S9. Dashed curves are calculated in the same way for hydrate-coated bubbles, but assuming the mass transfer coefficient is only 20% of its value for hydrate free bubbles. Results agree with the measured percentage loss in bubble size over a 150-cm rise for bubbles released in Monterey Bay. (Data taken from Rehder et al., 2009 as described in Text S9.) (b) Percentage of methane lost as a function of initial water depth, assuming the temperature correlation with water depth from Milkov and Sassen (2001) for the GOM. For the typical bubble radii at the sites in this study (1–5 mm), a loss of methane on the order of 1% can be expected for bubbles released with a methane shell relative to ~5% for hydrate-free bubbles.

$$C_0\left(\frac{\text{moles}}{\text{cm}^3}\right) = \frac{2.5\times10^{-8}}{z(\text{cm})}. \tag{7}$$

Equation 7 describes a rapidly decaying profile in which C_0 drops by four orders of magnitude in just the first 25 cm above the seafloor (Lapham et al., 2013), falling from ~10 mM to 1 μM (0.1 mmol/cm^3 to 1 nmol/cm^3). At ~10 m above a seep, measured C_0 values drop to 5–10 nM (5–10 pmol/cm^3; Garcia-Tigreros et al., 2021), equivalent to measured background levels of 10–20 nM (10–20 pm/cm^3; Gentz et al., 2014; Pohlman et al., 2017). Though we include Equation 7 profile of C_0 in our calculations, C_0 decays so steeply with rise height that methane loss results plotted at the z = 0–150 cm scale for Figure 15 are indistinguishable from those calculated assuming $C_0 = 0$ for all values of z.

Nonetheless, the elevated C_0 is important for catalyzing hydrate formation (Chen et al., 2014; Maini & Bishnoi, 1981; Ruppel & Waite, 2020; Warzinski et al., 2014) at the seafloor. Moreover, bubbles released from the seafloor bring with them a thin boundary layer of the relatively high C_0 bottom water. The boundary layer thickness is only on the order of $r^{-1/2}$ (Kang & Leal, 1988; Moore, 1963), but its high methane-content may facilitate shell growth on clean bubbles. In addition to dissolution of hydrate and bubbles, water-column methane at the near-seafloor environment can be supplied by dissolved methane flowing out of the seafloor (Levin et al., 2016; Torres et al., 2002), and by stationary hydrate-coated bubbles (e.g., bubbles circled in Figure 3b and noted in Figure 4b). However, these seep sources are often not strong enough to produce high methane concentrations over long distances.

Figure 15a shows the percentage of methane lost from bubbles during their first 150-cm rise from the seafloor. We compare the results with the bubble shrinkage rates measured by Rehder et al. (2002, 2009) in Monterey Bay. The modeling results are consistent with the field measurement for bubbles while they are hydrate-free (clean) and when they subsequently become hydrate-coated. This confirms that the assumption of $K_{\text{hydrate}} = 0.2 \cdot K_{\text{hydrate-free}}$ is indeed a viable approximation.

Similar to the hydrate shell analysis (Figure 14a), the results in Figure 15a monotonically decrease with increasing bubble radius. This is due to the volume-to-area ratio effect, where methane loss via dissolution scales with the surface area (r^2; Equation 6) but the total methane content scales with the bubble volume (r^3).

Figure 15 shows that hydrate-free bubbles contribute ~5% of their methane (solid lines) to the near-seafloor dissolved methane concentration, C_0. Though hydrate-coated bubbles contribute less methane over that initial 150-cm rise (dashed lines), the results indicate that dissolution occurs even for bubbles with hydrate shells. Consequently, the bubbles remaining fixed to the seafloor during the videos are also contributing dissolved methane to the near-seafloor environment.

For the relationship between bottom water temperature and depth in the GOM given by Milkov and Sassen (2001), the amount of methane loss is nearly independent of the water depth at which the bubble is released from the seafloor (Figure 15b). With increasing water depth, the rising pressure and falling temperature elevates both the total initial methane content (via increased gas density) and the driving force for dissolution (via increased solubility, C_S). When calculating methane loss on a percentage basis, the two effects nearly cancel.

Finally, we combine the hydrate shell formation effect (Figure 14) and the shielding effect (the difference between the solid and dashed curves in Figure 15), to calculate the total difference in methane content between hydrate-free and initially hydrate-coated bubbles after their 150-cm rise. The results, shown in Figure 16, are presented for both the static and dynamic hydrate shell assumption. The two endmembers provide the upper and lower bound of our estimates. We also plot the average of the two endmembers as a function of water depth. For typical GOM bubble sizes in this study (r = 1–5 mm), bubbles forming hydrate shells prior to their seafloor release will contain ~5% more methane than bubbles of equal initial volume that do not form shells prior to rising ~150 cm. This result is weakly dependent on seafloor depth in the GOM and should be applicable to any typical deep marine environment.

Seafloor observations presented here indicate bubbles within a single seep site can be released from the seafloor in either a hydrate-free (clean) or hydrate-shelled condition. Considering these two endmembers when implementing a dissolution model to track gas loss as a bubble rises provides a constraint on the initial amount of gas present in the bubble or bubble-plus-shell system, as well as how much gas dissolves in the first 1–2 m of bubble rise. The endmember consideration becomes more complex in a mixed-gas system.

As noted in Section 5.1, each gas component must be addressed individually because the partitioning of gas component between the gaseous and hydrate phases can differ significantly between components and between hydrate structures. The dissolution rate equation (Equation 6) must similarly be solved separately for each gas component. For a mixture of methane, ethane and propane, the general result calculated by Gros et al. (2020) is that diffusion occurs more slowly for the higher hydrocarbons, meaning ethane, and particularly propane can be carried higher into the water column by rising bubbles than can methane.

The decreased dissolution rate for higher hydrocarbons is due to a number of factors. Considering the parameters in the numerator of Equation 6, the mass transfer coefficient and solubility both decrease with increasing carbon number. The mass transfer coefficient depends on the diffusivity of the gas component (Text S9), and diffusivity values decrease measurably with increasing carbon number: Witherspoon and Saraf (1965) report the diffusivity for ethane is 19% lower, and for propane is 35% lower than that of methane. Solubility also decreases with increasing carbon number (Brooks et al., 1951). In the denominator, the bubble velocity for a mixed gas is also lower than for pure methane. However, as shown in Text S9, this reduction is only on the order of a few percent.

The full incorporation of oil and multi-gas mixture is beyond the scope of this work. However, using the Texas A&M Oil spill/Outfall Calculator (TAMOC), Gros et al. (2020) show that, for release depths of

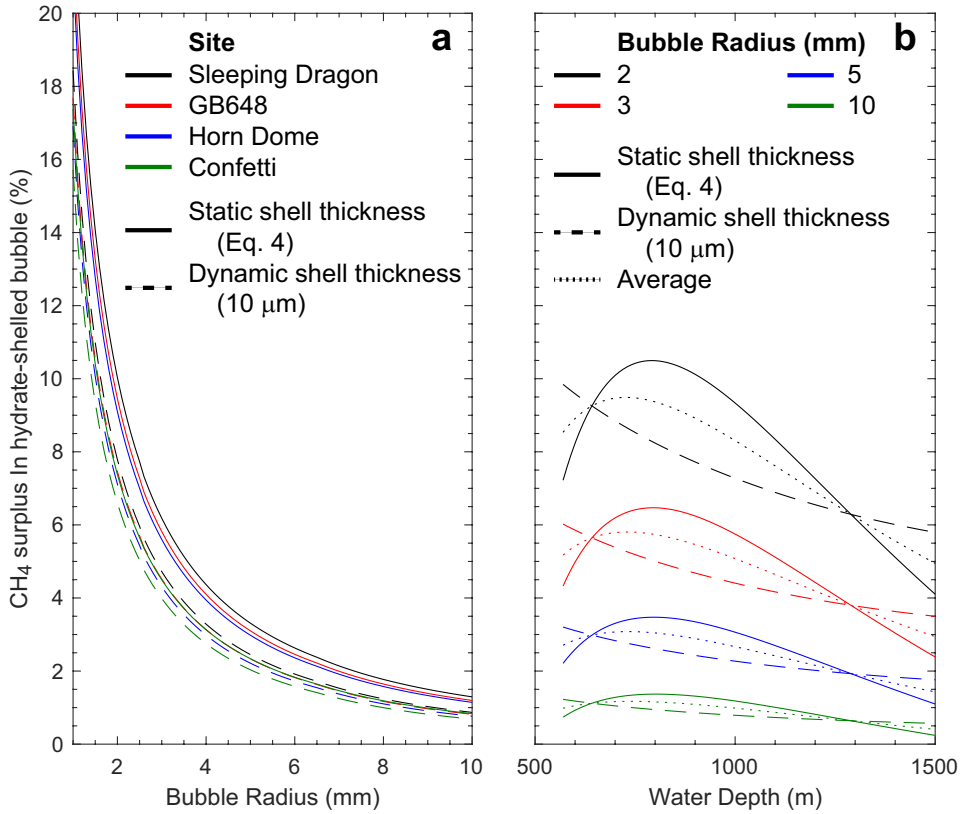

Figure 16. Total methane surplus after the initial 150-cm rise from the seafloor for an initially hydrate-shelled, spherical bubble relative to a hydrate-free bubble of initially equal volume. (a) Methane surplus dependence on bubble radius and shell thickness for the four GOM sites listed in Tables 1 and 2. (b) Methane surplus dependence on initial water depth, assuming the temperature correlation with water depth from Milkov and Sassen (2001) for the Gulf of Mexico. Dotted curves average the static and dynamic shell endmember results. After their initial 150-cm rise, bubbles released with a hydrate shell can be expected to have ~5% more methane than bubbles that do not acquire a shell until 150 cm above the seafloor.

~1,000 m in the GOM (approximately that of GB648 and HD), almost no methane will reach the sea surface; meanwhile, ~2.5% of the bubble's original ethane content, and 46% of the original propane content of a hypothetical 5 mm diameter bubble will reach the sea surface. The sensitivity of the TAMOC model to the initial gas content of bubbles highlights the importance of establishing the initial state of bubbles when released from the seafloor. The bottom-water videos presented here indicate that bubbles can become released in either hydrate-free or hydrate-coated state from a single site.

There are competing views on the role of oil in modifying the dissolution of methane and other hydrocarbon gases. Solomon et al. (2009) report that oily coatings would help preserve methane in rising bubbles, allowing methane communication to the surface mixing layer and even to the sea surface itself. Conversely, in their modeling of the GOM Macondo well blowout, Gros et al. (2020) indicate that methane would not reach the surface via bubbles and that oil droplets carried almost no methane, ethane, or propane at sea surface when released from a hypothesized 1,000 m water depth. Oil coatings are not the only preserving factor, however, and both studies point out the importance of upwelling in possibly enabling bubbles to transport methane to the sea surface.

6. Conclusions

Natural methane seeps display a diverse range of lithology, bubble release mechanisms and bubble release times. All these variabilities contribute to the complexity of how seep methane is delivered to the water column. In this study of seafloor seeps within the methane hydrate stability zone, emitted bubbles range

from 1 to 5 mm in radius, with 0%–100% of their surfaces coated with hydrate and shapes ranging from nearly spherical to irregular. Fluxes can also vary dramatically over short distances. At New England Seep 2, for example, we find that the estimated gas fluxes from individual emitters can differ by a factor of up to 6. Amongst these diverse behaviors, a few generalizations can be made: (a) more rapid bubble emitters tend to release smaller bubbles with little-to-no hydrate coating. Emission times exceeding 5 s/bubble tend to result in bubbles with significant hydrate coating, with full or nearly full coatings common for emission times greater than 10 s. (b) With increasing hydrate coverage on the bubble surface, bubbles released with oblong and irregular shapes become more common. (c) Within the hydrate stability zone, both hydrate-free and hydrate coated bubbles are produced at the seafloor, but, at ∼150 cm above the seafloor, most bubbles are hydrate-coated (Wang et al., 2016).

The observed diversity in how methane is released from seeps has implications for how that methane becomes distributed in the water column. Methane diffuses more rapidly out of the nearly hydrate-free bubbles due to the clean bubble's high mass-transfer rates. Though a hydrate shell reduces mass transfer rate, hydrate-coated bubbles with highly irregular shapes can still dissolve close to the seafloor due to the increased surface area and lower rise velocity. These methane contributions to the near-seafloor dissolved methane content, C_0, complement the direct delivery of dissolved-phase methane from the seabed (Levin et al., 2016; Torres et al., 2002) to create a localized microcosm of elevated C_0. The elevated C_0 levels decrease rapidly with height, reaching background levels within ∼10 m above the seep (Garcia-Tigreros et al., 2021), but are vital for promoting hydrate formation at, near, and within meters above the seafloor.

The water-column profile of C_0 decays so rapidly that C_0 can be set to 0 when calculating water column dissolution rates from rising bubbles. The hydrate shell formation history, however, should not be ignored. Even though the majority of the bubbles are hydrate-coated ∼150 cm above the seeps at these sites, bubbles initially released with a hydrate shell will have ∼5% more methane than initially hydrate-free bubbles of equal initial volume. Hydrate formation complicates dissolution calculations because surface area and rise velocity are not easily predicted for the irregular shapes observed for hydrate-coated bubbles. The mass transfer rate dependence on bubble shape and shell thickness is also poorly constrained. Over short rise distances, however, we show the McGinnis et al. (2006) observation that dissolution rates for hydrate-coated bubbles are 20% of the hydrate-free, clean bubble dissolution rates provides a satisfactory approach to calculating methane dissolution rate for hydrate-coated bubbles.

Acknowledgments
X. Fu acknowledges support from the Miller Fellowship during her time at U.C. Berkeley. W. Waite and C. Ruppel are supported by the United States Geological Survey (USGS) Coastal/Marine Hazards and Resources Program and the Energy Resources Program, with research conducted under USGS-Department of Energy interagency agreements DE-FE0023495 and 89243320SFE000013. This work benefited from NOAA's office of Ocean Exploration and Research, through research related to NOAA-USGS Interagency Agreement 16-0118 and the opportunities C. Ruppel was given to participate remotely in ROV dives on the United States Atlantic and GOM margins in 2013, 2014, and 2017. The authors thank S. Socolofsky and B. Wang for their assistance with the MC118 and GC600 data. They also thank A. Padilla and anonymous reviewers for their insightful comments that improved this article. Any use of trade, firm, or product name is for descriptive purposes only and does not imply endorsement by the United States Government.

Data Availability Statement

The Supporting Information S1 contains NOAA-OER seafloor video links. All other data used to produce the analysis in Figures 8, 12 and 14–16 are available on the Zenodo repository: https://doi.org/10.5281/zenodo.5178050.

References

Abe, Y., Abe, Y., Aya, I., & Yamane, K. (2007). The optical measurement of CO_2 clathrate hydrate membrane thickness. *Journal of Thermal Science and Technology*, *2*(1), 13–18. https://doi.org/10.1299/jtst.2.13

Akgerman, A., & Gainer, J. L. (1972). Predicting gas-liquid diffusivities. *Journal of Chemical & Engineering Data*, *17*(3), 372–377. https://doi.org/10.1021/je60054a008

Beaudoin, Y. C., Waite, W., Boswell, R., & Dallimore, S. R. (2014). *Frozen heat: A UNEP global outlook on methane gas hydrates* (Vol. 1). United Nations Environment Programme, GRID-Arendal.

Bernard, B. B., Brooks, J. M., & Sackett, W. M. (1976). Natural gas seepage in the Gulf of Mexico. *Earth and Planetary Science Letters*, *31*(1), 48–54. https://doi.org/10.1016/0012-821X(76)90095-9

Bigalke, N. K., Enstad, L. I.,Rehder, G., & Alendal, G. (2010). Terminal velocities of pure and hydrate coated CO_2 droplets and CH_4 bubbles rising in a simulated oceanic environment. *Deep Sea Research Part I: Oceanographic Research Papers*, *57*(9), 1102–1110. https://doi.org/10.1016/j.dsr.2010.05.008

Boetius, A., & Wenzhöfer, F. (2013). Seafloor oxygen consumption fuelled by methane from cold seeps. *Nature Geoscience*, *6*(9), 725–734. https://doi.org/10.1038/ngeo1926

Boewer, L., Nase, J., Paulus, M., Lehmkühler, F., Tiemeyer, S., Holz, S., et al. (2012). On the spontaneous formation of clathrate hydrates at water-guest interfaces. *Journal of Physical Chemistry*, *116*(15), 8548–8553. https://doi.org/10.1021/jp211784w

Boswell, R., Collett, T., Anderson, B., & Ruppel, C. (2010). Relative gas volume ratios for free gas and gas hydrate accumulations. *Fire in the Ice*, *10*(2), 9–11.

Boswell, R., Collett, T. S., Frye, M., Shedd, W., McConnell, D. R., & Shelander, D. (2012). Subsurface gas hydrates in the northern Gulf of Mexico. *Marine and Petroleum Geology*, *34*(1), 4–30. https://doi.org/10.1016/j.marpetgeo.2011.10.003

Brooks, J. M., Kennicutt, M. C., Fay, R. R., McDonald, T. J., & Sassen, R. (1984). Thermogenic gas hydrates in the Gulf of Mexico. *Science*, *225*(4660), 409. https://doi.org/10.1126/science.225.4660.409

Brooks, W. B., Gibbs, G. B., & McKetta, J. J. (1951). Mutual solubilities of light hydrocarbon-water systems. *Petroleum Refiner*, *30*(10).

Chatzievangelou, D., Aguzzi, J., Ogston, A., Suárez, A., & Thomsen, L. (2020). Visual monitoring of key deep-sea megafauna with an Internet Operated crawler as a tool for ecological status assessment. *Progress in Oceanography*, *184*, 102321. https://doi.org/10.1016/j.pocean.2020.102321

Chen, L. T., Sloan, E. D., Koh, C. A., & Sum, A. K. (2014). Methane hydrate formation and dissociation on suspended gas bubbles in water. *Journal of Chemical & Engineering Data*, *59*(4), 1045–1051. https://doi.org/10.1021/je400765a

Clift, R., Grace, J. R., & Weber, M. E. (1978). *Bubbles, drops, and particles*. Dover Publications, Inc.

Collett, T., Johnson, A., Knapp, C., & Boswell, R. (2009). Natural gas hydrates—A review. In T. Collett, A. Johnson, C. Knapp, & R. Boswell (Eds.), *Natural gas hydrates—Energy resource and associated geologic hazards* (pp. 146–220). AAPG Memoir 89. https://doi.org/10.1306/13201142m891602

Cook, A., Goldberg, D., & Kleinberg, R. L. (2008). Fracture-controlled gas hydrate systems in the northern Gulf of Mexico. *Marine and Petroleum Geology*, *25*, 932–941. https://doi.org/10.1016/j.marpetgeo.2008.01.013

Cranston, R., Ginsburg, G., Soloviev, V., & Lorenson, T. (1994). Gas venting and hydrate deposits in the Okhotsk Sea. *Bulletin of the Geological Society of Denmark*, *41*. https://doi.org/10.37570/bgsd-1995-41-08

Daigle, H., Cook, A., & Malinverno, A. (2018). Formation of massive hydrate deposits in Gulf of Mexico sand layers. *Fire in the Ice*, *18*(1), 1–3.

Davidson, L., & Amick, E. H., Jr. (1956). Formation of gas bubbles at horizontal orifices. *AIChE Journal*, *2*(3), 337–342. https://doi.org/10.1002/aic.690020309

Doya, C., Chatzievangelou, D., Bahamon, N., Purser, A., De Leo, F. C., Juniper, S. K., et al. (2017). Seasonal monitoring of deep-sea megabenthos in Barkley Canyon cold seep by internet operated vehicle (IOV). *PLoS ONE*, *12*(5). e0176917–e0176917. https://doi.org/10.1371/journal.pone.0176917

Duan, Z. H., & Mao, S. D. (2006). A thermodynamic model for calculating methane solubility, density and gas phase composition of methane-bearing aqueous fluids from 273 to 523 K and from 1 to 2000 bar. *Geochimica et Cosmochimica Acta*, *70*(13), 3369–3386. https://doi.org/10.1016/j.gca.2006.03.018

Duan, Z. H., Moller, N., Greenberg, J., & Weare, J. H. (1992). The prediction of methane solubility in natural-waters to high ionic-strength from 0°C to 250°C and from 0 to 1600 bar. *Geochimica et Cosmochimica Acta*, *56*(4), 1451–1460. https://doi.org/10.1016/0016-7037(92)90215-5

Egorov, V. N., Polikarpov, G. G., Gulin, S. B., Artemov, Y. G., Stokozov, N. A., & Kostova, S. K. (2003). Present-day views on the environment-forming and ecological role of the Black Sea methane gas seeps. *Marine Ecology Journal*, *2*(3), 5–26.

Embley, R., Raineault, N., Merle, S., Baumberger, T., Seabrook, S., & Hammond, S. (2016). Water column and cold seep exploration of the Cascadia margin. *Oceanography*, *30*(1), 94. https://doi.org/10.5670/oceanog.2017.supplement

Epstein, P. S., & Plesset, M. S. (1950). On the stability of gas bubbles in liquid-gas solutions. *The Journal of Chemical Physics*, *18*(11), 1505–1509. https://doi.org/10.1063/1.1747520

Fisher, C. R., MacDonald, I. R., Sassen, R., Young, C. M., Macko, S. A., Hourdez, S., et al. (2000). Methane ice worms: Hesiocaeca methanicola colonizing fossil fuel reserves. *Naturwissenschaften*, *87*(4), 184–187. https://doi.org/10.1007/s001140050700

Fisher, C. R., Roberts, H., Cordes, E., & Bernard, B. (2015). Cold seeps and associated communities of the Gulf of Mexico. *Oceanography*, *20*(4), 118–129. https://doi.org/10.5670/oceanog.2007.12

Fofonoff, N. P. (1985). Physical properties of seawater—A new salinity scale and equation of state for seawater. *Journal of Geophysical Research*, *90*(Nc2), 3332–3342. https://doi.org/10.1029/jc090ic02p03332

Frye, M. (2008). *Preliminary evaluation of in-place gas hydrate resources: Gulf of Mexico Outer Continental Shelf (Rep. MMS 2008-004, Minerals Management Service, OCS Report MMS 2008-004)*. Retrieved from https://www.boem.gov/sites/default/files/documents//MMS2008-004.pdf

Fu, X., Cueto-Felgueroso, L., & Juanes, R. (2018). Nonequilibrium thermodynamics of hydrate growth on a gas-liquid interface. *Physical Review Letters*, *120*(14), 144501. https://doi.org/10.1103/PhysRevLett.120.144501

Fu, X., Jimenez-Martinez, J., Nguyen, T. P., Carey, J. W., Viswanathan, H., Cueto-Felgueroso, L., & Juanes, R. (2020). Crustal fingering facilitates free-gas methane migration through the hydrate stability zone. *Proceedings of the National Academy of Sciences of the United States of America*, *117*(50), 31660–31664. https://doi.org/10.1073/pnas.2011064117

Fu, X., Waite, W. F., Cueto-Felgueroso, L., & Juanes, R. (2019). Xenon hydrate as an analog of methane hydrate in geologic systems out of thermodynamic equilibrium. *Geochemistry, Geophysics, Geosystems*, *20*, 2462–2472. https://doi.org/10.1029/2019GC008250

Garcia-Tigreros, F., & Kessler, J. D. (2018). Limited acute influence of aerobic methane oxidation on ocean carbon dioxide and pH in Hudson Canyon, Northern U.S. Atlantic margin. *Journal of Geophysical Research: Biogeosciences*, *123*(7), 2135–2144. https://doi.org/10.1029/2018JG004384

Garcia-Tigreros, F., Leonte, M., Ruppel, C. D., Ruiz-Angulo, A., Joung, D. J., Young, B., & Kessler, J. D. (2021). Estimating the impact of seep methane oxidation on ocean pH and dissolved inorganic radiocarbon along the U.S. Mid-Atlantic Bight. *Journal of Geophysical Research: Biogeosciences*, *126*(1), e2019JG005621. https://doi.org/10.1029/2019JG005621

Gentz, T., Damm, E., Schneider von Deimling, J., Mau, S., McGinnis, D. F., & Schlüter, M. (2014). A water column study of methane around gas flares located at the West Spitsbergen continental margin. *Continental Shelf Research*, *72*, 107–118. https://doi.org/10.1016/j.csr.2013.07.013

Graves, C. A., Steinle, L., Rehder, G., Niemann, H., Connelly, D. P., Lowry, D., et al. (2015). Fluxes and fate of dissolved methane released at the seafloor at the landward limit of the gas hydrate stability zone offshore western Svalbard. *Journal of Geophysical Research: Oceans*, *120*(9), 6185–6201. https://doi.org/10.1002/2015JC011084

Gros, J., Arey, J. S., Socolofsky, S. A., & Dissanayake, A. L. (2020). Dynamics of live oil droplets and natural gas bubbles in deep water. *Environmental Science & Technology*, *54*(19), 11865–11875. https://doi.org/10.1021/acs.est.9b06242

Hayama, H., Fukuzawa, K., Yasuda, K., & Ohmura, R. (2017). Interfacial tension between (methane+ethane+propane) gas mixture and water from 283.2 K to 298.2 K under up to 10 MPa. *The Journal of Chemical Thermodynamics*, *108*, 71–75. https://doi.org/10.1016/j.jct.2017.01.007

Heintz, M. B., Mau, S., & Valentine, D. L. (2012). Physical control on methanotrophic potential in waters of the Santa Monica Basin, Southern California. *Limnology and Oceanography*, *57*(2), 420–432. https://doi.org/10.4319/lo.2012.57.2.0420

Helgerud, M. B., Waite, W. F., Kirby, S. H., & Nur, A. (2009). Elastic wave speeds and moduli in polycrystalline ice Ih, sI methane hydrate, and sII methane-ethane hydrate. *Journal of Geophysical Research*, *114*, B02212. https://doi.org/10.1029/2008JB006132

Hollebone, B. (2011). Chapter 4—Measurement of oil physical properties. In M. Fingas (Ed.), *Oil spill science and technology* (pp. 63–86). Gulf Professional Publishing. https://doi.org/10.1016/B978-1-85617-943-0.10004-8

Hornbach, M. J., Ruppel, C., & Van Dover, C. L. (2007). Three-dimensional structure of fluid conduits sustaining an active deep marine cold seep. *Geophysical Research Letters*, *34*, L05601. https://doi.org/10.01029/02006GL028859

Hovland, M., Judd, A. G., & Burke, R. A. (1993). The global flux of methane from shallow submarine sediments. *Chemosphere*, *26*(1), 559–578. https://doi.org/10.1016/0045-6535(93)90442-8

Hutchinson, D. R., Ruppel, C. D., Roberts, H. H., Carney, R. S., & Smith, M. A. (2011). Gas hydrates in the Gulf of Mexico. In N. A. Buster & C. W. Holmes (Eds.), *Gulf of Mexico origin, waters, and biota* (pp. 247–275). Texas A&M University Press.

Johnson, H. P., Miller, U. K., Salmi, M. S., & Solomon, E. A. (2015). Analysis of bubble plume distributions to evaluate methane hydrate decomposition on the continental slope. *Geochemistry, Geophysics, Geosystems*, *16*(11), 3825–3839. https://doi.org/10.1002/2015GC005955

Joye, S. B., Boetius, A., Orcutt, B. N., Montoya, J. P., Schulz, H. N., Erickson, M. J., & Lugo, S. K. (2004). The anaerobic oxidation of methane and sulfate reduction in sediments from Gulf of Mexico cold seeps. *Chemical Geology*, *205*(3), 219–238. https://doi.org/10.1016/j.chemgeo.2003.12.019

Jung, J. W., & Santamarina, J. C. (2011). Hydrate adhesive and tensile strengths. *Geochemistry, Geophysics, Geosystems*, *12*(8). https://doi.org/10.1029/2010gc003495

Juniper, S. K., Matabos, M., Mihály, S., Ajayamohan, R. S., Gervais, F., & Bui, A. O. V. (2013). A year in Barkley Canyon: A time-series observatory study of mid-slope benthos and habitat dynamics using the NEPTUNE Canada network, *Deep Sea Research Part II: Topical Studies in Oceanography*, *92*, 114–123. https://doi.org/10.1016/j.dsr2.2013.03.038

Kang, I. S., & Leal, L. G. (1988). The drag coefficient for a spherical bubble in a uniform streaming flow. *The Physics of Fluids*, *31*(2), 233–237. https://doi.org/10.1063/1.866852

Kennedy, B., Messing, C., & Amon, D. (2019). *Oceanographic data collected during the EX1711 Gulf of Mexico Mapping (ROV & Mapping) expedition on NOAA Ship OKEANOS EXPLORER in the Gulf of Mexico from 2017-11-29 to 2017-12-21 (NCEI Accession 0170751)*. NOAA National Centers for Environmental Information. https://doi.org/10.25921/qsmk-bj73

Kennicutt, M. C. (2017). Oil and gas seeps in the Gulf of Mexico. In C. H. Ward (Ed.), *Habitats and biota of the Gulf of Mexico: Before the deepwater horizon oil spill: Volume 1: Water quality, sediments, sediment contaminants, oil and gas seeps, coastal habitats, offshore plankton and benthos, and shellfish* (pp. 275–358). Springer. https://doi.org/10.1007/978-1-4939-3447-8_5

Kessler, J. D., Valentine, D. L., Redmond, M. C., & Du, M. R. (2011). A persistent oxygen anomaly reveals the fate of spilled methane in the deep Gulf of Mexico. *Science*, *332*(6033). https://doi.org/10.1126/science.1203428

Kramer, K. V., & Shedd, W. W. (2017). A 1.4-billion-pixel map of the Gulf of Mexico seafloor. *Eos*, *98*. https://doi.org/10.1029/2017EO073557

Kvenvolden, K. A., Lorenson, T. D., & Reeburgh, W. S. (2001). Attention turns to naturally occurring methane seepage. *Eos, Earth and Space Science News*, *82*(40), 457–457. https://doi.org/10.1029/01EO00275

Lapham, L., Wilson, R., Riedel, M., Paull, C. K., & Holmes, M. E. (2013). Temporal variability of in situ methane concentrations in gas hydrate-bearing sediments near Bullseye Vent, Northern Cascadia Margin. *Geochemistry, Geophysics, Geosystems*, *14*(7), 2445–2459. https://doi.org/10.1002/ggge.20167

Lei, L., Seol, Y., & Myshakin, E. M. (2019). Methane hydrate film thickening in porous media. *Geophysical Research Letters*, *46*(20), 11091–11099. https://doi.org/10.1029/2019gl084450

Leifer, I., & Culling, D. (2010). Formation of seep bubble plumes in the Coal Oil Point seep field. *Geo-Marine Letters*, *30*(3), 339–353. https://doi.org/10.1007/s00367-010-0187-x

Leifer, I., & Patro, R. K. (2002). The bubble mechanism for methane transport from the shallow sea bed to the surface: A review and sensitivity study. *Continental Shelf Research*, *22*(16), 2409–2428. https://doi.org/10.1016/S0278-4343(02)00065-1

Lemmon, E. W., McLinden, M. O., & Friend, D. G. (2016). Thermophysical properties of fluid systems. In P. J. Linstrom & W. G. Mallard (Eds.), *NIST chemistry WebBook (NIST Standard Reference Database Number 69)*. National Institute of Standards and Technology.

Leonte, M., Ruppel, C. D., Ruiz-Angulo, A., & Kessler, J. D. (2020). Surface methane concentrations along the mid-Atlantic Bight driven by aerobic subsurface production rather than seafloor gas seeps. *Journal of Geophysical Research: Oceans*, *125*(5), e2019JC015989. https://doi.org/10.1029/2019JC015989

Leonte, M., Wang, B., Socolofsky, S. A., Mau, S., Breier, J. A., & Kessler, J. D. (2018). Using carbon isotope fractionation to constrain the extent of methane dissolution into the water column surrounding a natural hydrocarbon gas seep in the Northern Gulf of Mexico. *Geochemistry, Geophysics, Geosystems*, *19*(11), 4459–4475. https://doi.org/10.1029/2018GC007705

Levin, L. A. (2005). Ecology of cold seep sediments: Interactions of fauna with flow, chemistry and microbes. In R. N. Gibson, R. J. A. Atkinson, & J. D. M. Gordon (Eds.), *Oceanography and marine biology: An annual review* (pp. 1–46). CRC Press; Taylor & Francis Group. https://doi.org/10.1201/9781420037449

Levin, L. A., Baco, A. R., Bowden, D. A., Colaco, A., Cordes, E. E., Cunha, M. R., et al. (2016). Hydrothermal vents and methane seeps: Rethinking the sphere of influence. *Frontiers in Marine Science*, *3*(72). https://doi.org/10.3389/fmars.2016.00072

Li, C., & Huang, T. (2016). Simulation of gas bubbles with gas hydrates rising in deep water. *Ocean Engineering*, *112*, 16–24. https://doi.org/10.1016/j.oceaneng.2015.12.002

Li, H., Liu, Z., Chen, J., Sun, B., Guo, Y., & He, H. (2017). Correlation of aspect ratio and drag coefficient for hydrate-film-covered methane bubbles in water. *Experimental Thermal and Fluid Science*, *88*, 554–565. https://doi.org/10.1016/j.expthermflusci.2017.07.009

Li, S.-L., Sun, C.-Y., Chen, G.-J., Li, Z.-Y., Ma, Q.-L., Yang, L.-Y., & Sum, A. K. (2014). Measurements of hydrate film fracture under conditions simulating the rise of hydrated gas bubbles in deep water. *Chemical Engineering Science*, *116*, 109–117. https://doi.org/10.1016/j.ces.2014.04.009

Li, S.-L., Sun, C.-Y., Liu, B., Feng, X.-J., Li, F.-G., Chen, L.-T., & Chen, G.-J. (2013). Initial thickness measurements and insights into crystal growth of methane hydrate film. *AIChE Journal*, *59*(6), 2145–2154. https://doi.org/10.1002/aic.13987

Liu, Z., Sun, B., Wang, Z., & Chen, L. (2019). New mass-transfer model for predicting hydrate film thickness at the gas-liquid interface under different thermodynamics-hydrodynamics-saturation conditions. *Journal of Physical Chemistry*, *123*(34), 20838–20852. https://doi.org/10.1021/acs.jpcc.9b03843

Lloyd, K. G., Albert, D. B., Biddle, J. F., Chanton, J., Pizarro, O., & Teske, A. (2010). Spatial structure and activity of sedimentary microbial communities underlying a Beggiatoa spp. mat in a Gulf of Mexico hydrocarbon seep. *PLoS ONE*, *5*(1), e8738. https://doi.org/10.1371/journal.pone.0008738

Lobecker, E., Austin, J., & Farrington, S. (2019). *Oceanographic data and ROV dive-related multimedia and information collected during the EX1402L3 (Gulf of Mexico mapping and ROV exploration) expedition on NOAA Ship OKEANOS EXPLORER in the Gulf of Mexico from 2014-04-10 to 2014-05-01 (NCEI accession 0157088)*. NOAA National Centers for Environmental Information. https://doi.org/10.7289/v5nc5z7d

Maini, B. B., & Bishnoi, P. R. (1981). Experimental investigation of hydrate formation behaviour of a natural gas bubble in a simulated deep sea environment. *Chemical Engineering Science*, *36*, 183–189. https://doi.org/10.1016/0009-2509(81)80062-0

McGinnis, D. F., Greinert, J., Artemov, Y., Beaubien, S. E., & Wuest, A. (2006). Fate of rising methane bubbles in stratified waters: How much methane reaches the atmosphere? *Journal of Geophysical Research*, *111*(C9). https://doi.org/10.1029/2005jc003183

McVeigh, D., Skarke, A., Dekas, A. E., Borrelli, C., Hong, W. L., Marlow, J. J., et al. (2018). Characterization of benthic biogeochemistry and ecology at three methane seep sites on the Northern US Atlantic margin. *Deep-Sea Research Part II: Topical Studies in Oceanography*, *150*, 41–56. https://doi.org/10.1016/j.dsr2.2018.03.001

Merle, S., & Embley, R. (2016). *NA72-Seeps and ecosystems of the Cascadia margin, June 1–20, 2016 Victoria BC, Canada to San Francisco CA, USA (Cruise Report of the E/V Nautilus)*. (p. 278).

Merle, S., Embley, R., Johnson, H., Lau, T.-K., Phrampus, B., Raineault, N., & Gee, L. (2021). Distribution of methane plumes on Cascadia margin and implications for the landward limit of methane hydrate stability. *Frontiers of Earth Science*, *9*. https://doi.org/10.3389/feart.2021.531714

Milkov, A. V., & Sassen, R. (2001). Estimate of gas hydrate resource, northwestern Gulf of Mexico continental slope. *Marine Geology*, *179*(1–2), 71–83. https://doi.org/10.1016/s0025-3227(01)00192-x

Moore, D. W. (1963). The boundary layer on a spherical gas bubble. *Journal of Fluid Mechanics*, *16*(2), 161–176. https://doi.org/10.1017/s0022112063000665

Myhre, C. L., Ferré, B., Platt, S. M., Silyakova, A., Hermansen, O., Allen, G., et al. (2016). Extensive release of methane from Arctic seabed west of Svalbard during summer 2014 does not influence the atmosphere. *Geophysical Research Letters*, *43*(9), 4624–4631. https://doi.org/10.1002/2016gl068999

Oguz, H. N., & Prosperetti, A. (1993). Dynamics of bubble growth and detachment from a needle. *Journal of Fluid Mechanics*, *257*, 111–145. https://doi.org/10.1017/s0022112093003015

Olsen, J. E., Dunnebier, D., Davies, E. J., Skjetne, P., & Morud, J. (2017). Mass transfer between bubbles and seawater. *Chemical Engineering Science*, *161*, 308–315. https://doi.org/10.1016/j.ces.2016.12.047

Olsen, J. E., Krause, D. F., Davies, E. J., & Skjetne, P. (2019). Observations of rising methane bubbles in Trondheimsfjord and its implications to gas dissolution. *Journal of Geophysical Research: Oceans*, *124*(3), 1399–1409. https://doi.org/10.1029/2018jc013978

Orcutt, B., Boetius, A., Elvert, M., Samarkin, V., & Joye, S. B. (2005). Molecular biogeochemistry of sulfate reduction, methanogenesis and the anaerobic oxidation of methane at Gulf of Mexico cold seeps. *Geochimica et Cosmochimica Acta*, *69*(17), 4267–4281. https://doi.org/10.1016/j.gca.2005.04.012

Padilla, A. M., & Weber, T. C. (2021). Acoustic backscattering observations from non-spherical gas bubbles with ka between 0.03 and 4.4. *Journal of the Acoustical Society of America*, *149*(4), 2504–2519. https://doi.org/10.1121/10.0004246

Paull, C. K., Ussler, W., & Dillon, W. P. (2000). Potential role of gas hydrate decomposition in generating submarine slope failures. In M. D. Max (Ed.), *Natural gas hydrate in oceanic and permafrost environments* (pp. 149–156). Kluwer Academic Publishers.

Phrampus, B. J., Lee, T. R., & Wood, W. T. (2020). A global probabilistic prediction of cold seeps and associated seafloor fluid expulsion anomalies (SEAFLEAs). *Geochemistry, Geophysics, Geosystems*, *21*(1), e2019GC008747. https://doi.org/10.1029/2019GC008747

Pinczewski, W. V. (1981). The formation and growth of bubbles at a submerged orifice. *Chemical Engineering Science*, *36*(2), 405–411. https://doi.org/10.1016/0009-2509(81)85021-X

Pohlman, J. W., Greinert, J., Ruppel, C., Silyakova, A., Vielstädte, L., Casso, M., et al. (2017). Enhanced CO2 uptake at a shallow Arctic Ocean seep field overwhelms the positive warming potential of emitted methane. *Proceedings of the National Academy of Sciences of the United States of America*, *114*(21), 5355. https://doi.org/10.1073/pnas.1618926114

Purser, A., Thomsen, L., Barnes, C., Best, M., Chapman, R., Hofbauer, M., et al. (2013). Temporal and spatial benthic data collection via an internet operated deep sea crawler. *Methods in Oceanography*, *5*. https://doi.org/10.1016/j.mio.2013.07.001

Quattrini, A. M., Nizinski, M. S., Chaytor, J. D., Demopoulos, A. W., Roark, E. B., France, S. C., et al. (2015). Exploration of the canyon-incised continental margin of the northeastern United States reveals dynamic habitats and diverse communities. *PloS One*, *10*(10), e0139904. https://doi.org/10.1371/journal.pone.0139904

Redmond, M. C., & Valentine, D. L. (2012). Natural gas and temperature structured a microbial community response to the deepwater horizon oil spill. *Proceedings of the National Academy of Sciences of the United States of America*, *109*(50), 20292–20297. https://doi.org/10.1073/pnas.1108756108

Reeburgh, W. S. (1976). Methane consumption in Cariaco Trench waters and sediments. *Earth and Planetary Science Letters*, *28*(3), 337–344. https://doi.org/10.1016/0012-821X(76)90195-3

Reeburgh, W. S. (2007). Oceanic methane biogeochemistry. *Chemical Reviews*, *107*(2), 486–513. https://doi.org/10.1021/cr050362v

Rehder, G., Brewer, P. W., Peltzer, E. T., & Friederich, G. (2002). Enhanced lifetime of methane bubble streams within the deep ocean. *Geophysical Research Letters*, *29*(15), 21-1–21-4. https://doi.org/10.1029/2001gl013966

Rehder, G., Keir, R. S, Suess, E., & Rhein, M. (1999). Methane in the northern Atlantic controlled by microbial oxidation and atmospheric history. *Geophysical Research Letters*, *26*(5), 587–590. https://doi.org/10.1029/1999GL900049

Rehder, G., Leifer, I., Brewer, P. G., Friederich, G., & Peltzer, E. T. (2009). Controls on methane bubble dissolution inside and outside the hydrate stability field from open ocean field experiments and numerical modeling. *Marine Chemistry*, *114*(1–2), 19–30. https://doi.org/10.1016/j.marchem.2009.03.004

Riedel, M., Scherwath, M., Römer, M., Veloso, M., Heesemann, M., & Spence, G. D. (2018). Distributed natural gas venting offshore along the Cascadia margin. *Nature Communications*, *9*(1), 3264. https://doi.org/10.1038/s41467-018-05736-x

Roberts, H. H. (2001). Fluid and gas expulsion on the Northern Gulf of Mexico continental slope: Mud-prone to mineral-prone responses. In C. K. Paull & W. P. Dillon (Eds.), *Natural gas hydrates: Occurrence, distribution and detection* (Vol. 124, pp. 145–161). American Geophysical Union.

Ruppel, C. D., & Amon, D. (2017). *Ice worms and gas hydrate-encased bubble tubes*. U.S. Geological Survey.

Ruppel, C. D., & Kessler, J. D. (2017). The interaction of climate change and methane hydrates. *Reviews of Geophysics*, *55*, 126–168. https://doi.org/10.1002/2016rg000534

Ruppel, C. D., & Waite, W. F. (2020). Timescales and processes of methane hydrate formation and breakdown, with application to geologic systems. *Journal of Geophysical Research: Solid Earth*, *125*(8), e2018JB016459. https://doi.org/10.1029/2018jb016459

Sachs, W., & Meyn, V. (1995). Pressure and temperature dependence of the surface tension in the system natural gas/water principles of investigation and the first precise experimental data for pure methane/water at 25°C up to 46.8 MPa. *Colloids and Surfaces A: Physicochemical and Engineering Aspects*, *94*(2), 291–301. https://doi.org/10.1016/0927-7757(94)03008-1

Sassen, R., Milkov, A. V., Ozgul, E., Roberts, H. H., Hunt, J. L., Beeunas, M. A., et al. (2003). Gas venting and subsurface charge in the Green Canyon area, Gulf of Mexico continental slope: Evidence of a deep bacterial methane source? *Organic Geochemistry*, *34*(10), 1455–1464. https://doi.org/10.1016/S0146-6380(03)00135-9

Sassen, R., Roberts, H. H., Carney, R., Milkov, A. V., DeFreitas, D. A., Lanoil, B., & Zhang, C. (2004). Free hydrocarbon gas, gas hydrate, and authigenic minerals in chemosynthetic communities of the northern Gulf of Mexico continental slope: Relation to microbial processes. *Chemical Geology*, *205*(3), 195–217. https://doi.org/10.1016/j.chemgeo.2003.12.032

Seabrook, S., De Leo, F. C., & Thurber, A. R. (2019). Flipping for food: The use of a methane seep by tanner crabs (Chionoecetes tanneri). *Frontiers in Marine Science*, *6*(43). https://doi.org/10.3389/fmars.2019.00043

Shank, T., Quattrini, A., Bingham, B., & Elliott, K. (2014). *New England seep 2*. NOAA Office of Exploration and Research.

Skarke, A., Ruppel, C., Kodis, M., Brothers, D., & Lobecker, E. (2014). Widespread methane leakage from the sea floor on the northern US Atlantic margin. *Nature Geoscience*, *7*(9), 657–661. https://doi.org/10.1038/ngeo2232

Sloan, E. D., & Koh, C. A. (2007). *Clathrate hydrates of natural gases* (3rd ed., p. 721). CRC Press.

Solomon, E. A., Kastner, M., MacDonald, I. R., & Leifer, I. (2009). Considerable methane fluxes to the atmosphere from hydrocarbon seeps in the Gulf of Mexico. *Nature Geoscience*, *2*(8), 561–565. https://doi.org/10.1038/ngeo574

Soloviev, A. V., Haus, B. K., McGauley, M. G., Dean, C. W., Ortiz-Suslow, D. G., Laxague, N. J. M., & Özgökmen, T. M. (2016). Surface dynamics of crude and weathered oil in the presence of dispersants: Laboratory experiment and numerical simulation. *Journal of Geophysical Research: Oceans*, *121*, 3502–3516. https://doi.org/10.1002/2015JC011533

Sparrow, K. J., Kessler, J. D., Southon, J. R., Garcia-Tigreros, F., Schreiner, K. M., Ruppel, C. D., et al. (2018). Limited contribution of ancient methane to surface waters of the U.S. Beaufort Sea shelf. *Science Advances*, *4*(1), eaao4842. https://doi.org/10.1126/sciadv.aao4842

Sundquist, E. T., & Visser, K. (2003). The geologic history of the carbon cycle. In W. Schlesinger, Holland, H. D., & Turekian, K. K. (Eds.), *Biochemistry: Treatise on geochemistry* (pp. 425–472). Elsevier. https://doi.org/10.1016/b0-08-043751-6/08133-0

Sychev, V. V., Vasserman, A. A., Zagoruchenko, V. A., Kozlov, A. D., Spiridonov, G. A., & Tsymarny, V. A. (1987). *Thermodynamic properties of methane* (p. 341). Hemisphere Publishing Corporation.

Taylor, C. J., Miller, K. T., Koh, C. A., & Sloan, E. D. (2007). Macroscopic investigation of hydrate film growth at the hydrocarbon/water interface. *Chemical Engineering Science*, *62*(23), 6524–6533. https://doi.org/10.1016/j.ces.2007.07.038

Thomsen, L., Barnes, C., Best, M., Chapman, R., Pirenne, B., Thomson, R., & Vogt, J. (2012). Ocean circulation promotes methane release from gas hydrate outcrops at the NEPTUNE Canada Barkley Canyon node. *Geophysical Research Letters*, *39*(16). https://doi.org/10.1029/2012gl052462

Tishchenko, P., Hensen, C., Wallmann, K., & Wong, C. S. (2005). Calculation of the stability and solubility of methane hydrate in seawater. *Chemical Geology*, *219*(1–4), 37–52. https://doi.org/10.1016/j.chemgeo.2005.02.008

Topham, D. R. (1984a). The formation of gas hydrates on bubbles of hydrocarbon gases rising in seawater. *Chemical Engineering Science*, *39*, 821–828. https://doi.org/10.1016/0009-2509(84)85051-4

Topham, D. R. (1984b). The modeling of hydrocarbon bubble plumes to include gas hydrate formation. *Chemical Engineering Science*, *39*(11), 1613–1622. https://doi.org/10.1016/0009-2509(84)80088-3

Torres, M. E., McManus, J., Hammond, D. E., de Angelis, M. A., Heeschen, K. U., Colbert, S. L., et al. (2002). Fluid and chemical fluxes in and out of sediments hosting methane hydrate deposits on Hydrate Ridge, OR, I: Hydrological provinces. *Earth and Planetary Science Letters*, *201*(3–4), 525–540. https://doi.org/10.1016/S0012-821X(02)00733-1

Valentine, D. L., Blanton, D. C., Reeburgh, W. S., & Kastner, M. (2001). Water column methane oxidation adjacent to an area of active hydrate dissociation, Eel River Basin. *Geochimica et Cosmochimica Acta*, *65*(16), 2633–2640. https://doi.org/10.1016/S0016-7037(01)00625-1

Van Dover, C. L., Aharon, P., Bernhard, J. M., Caylor, E., Doerries, M., Flickinger, W., et al. (2003). Blake ridge methane seeps: Characterization of a soft-sediment, chemo synthetically based ecosystem. *Deep-Sea Research Part I Oceanographic Research Papers*, *50*(2), 281–300. https://doi.org/10.1016/S0967-0637(02)00162-0

Wang, B., Jun, I., Socolofsky, S. A., DiMarco, S. F., & Kessler, J. D. (2020). Dynamics of gas bubbles from a submarine hydrocarbon Seep Within the hydrate stability zone. *Geophysical Research Letters*, *47*(18), e2020GL089256. https://doi.org/10.1029/2020GL089256

Wang, B. B., & Socolofsky, S. A. (2015). A deep-sea, high-speed, stereoscopic imaging system for in situ measurement of natural seep bubble and droplet characteristics. *Deep-Sea Research Part I Oceanographic Research Papers*, *104*, 134–148. https://doi.org/10.1016/j.dsr.2015.08.001

Wang, B. B., Socolofsky, S. A., Breier, J. A., & Seewald, J. S. (2016). Observations of bubbles in natural seep flares at MC 118 and GC 600 using in situ quantitative imaging. *Journal of Geophysical Research: Oceans*, *121*(4), 2203–2230. https://doi.org/10.1002/2015jc011452

Warzinski, R. P., Lynn, R., Haljasmaa, I., Leifer, I., Shaffer, F., Anderson, B. J., & Levine, J. S. (2014). Dynamic morphology of gas hydrate on a methane bubble in water: Observations and new insights for hydrate film models. *Geophysical Research Letters*, *41*(19), 6841–6847. https://doi.org/10.1002/2014gl061665

Weast, R. C. (1987). *CRC handbook of chemistry and physics* (68th ed.). CRC Press, Inc.

Westbrook, G. K., Thatcher, K. E., Rohling, E. J., Piotrowski, A. M., Pälike, H., Osborne, A. H., et al. (2009). Escape of methane gas from the seabed along the West Spitsbergen continental margin. *Geophysical Research Letters*, *36*. https://doi.org/10.1029/2009gl039191

Whiticar, M. J. (1999). Carbon and hydrogen isotope systematics of bacterial formation and oxidation of methane. *Chemical Geology*, *161*(1), 291–314. https://doi.org/10.1016/S0009-2541(99)00092-3

Witherspoon, P. A., & Saraf, D. N. (1965). Diffusion of methane, ethane, propane, and n-butane in water from 25 to 43°. *Journal of Physical Chemistry*, *69*(11), 3752–3755. https://doi.org/10.1021/j100895a017

Worrall, D. M., & Snelson, S. (1989). Evolution of the northern Gulf of Mexico, with emphasis on Cenozoic growth faulting and the role of salt. In A. W. Bally & A. R. Palmer (Eds.), *The geology of North America—An overview*. Geological Society of America. https://doi.org/10.1130/DNAG-GNA-A.97

Wüest, A., Brooks, N. H., & Imboden, D. M. (1992). Bubble plume modeling for lake restoration. *Water Resources Research*, *28*(12), 3235–3250. https://doi.org/10.1029/92wr01681

Yapa, P. D., Dasanayaka, L. K., Bandara, U. C., & Nakata, K. (2010). A model to simulate the transport and fate of gas and hydrates released in deepwater. *Journal of Hydraulic Research*, *48*(5), 559–572. https://doi.org/10.1080/00221686.2010.507010

Yin, Z. Y., Khurana, M., Tan, H. K., & Linga, P. (2018). A review of gas hydrate growth kinetic models. *Chemical Engineering Journal*, *342*, 9–29. https://doi.org/10.1016/j.cej.2018.01.120

Zatsepina, O. Y., & Buffett, B. A. (1997). Phase equilibrium of gas hydrate: Implications for the formation of hydrate in the deep-sea floor. *Geophysical Research Letters*, *24*(13), 1567–1570. https://doi.org/10.1029/97GL01599

Zheng, L., & Yapa, P. D. (2002). Modeling gas dissolution in deepwater oil/gas spills. *Journal of Marine Systems*, *31*(4), 299–309. https://doi.org/10.1016/S0924-7963(01)00067-7

References From the Supporting Information

Jamialahmadi, M., Branch, C., & Müller-Steinhagen, J. (1994). Terminal bubble rise velocity in liquids. *Transactions of the Institution of Chemical Engineers*, *72*, 119–122.

Liu, N., Yang, Y., Wang, J., Ju, B., Brantson, E. T., Tian, Y., et al. (2020). Experimental investigations of single bubble rising in static Newtonian fluids as a function of temperature using a modified drag coefficient. *Natural Resources Research*, *29*(3), 2209–2226. https://doi.org/10.1007/s11053-019-09537-x